ORNL/TM-2023/2999

Preliminary Feasibility of Printing, Microstructure Analysis and Mechanical Performance of a Down Selected Ni Alloy

Sebastien Dryepondt
Stephen Taller
Fred List
Zachary Snow

July 2023

M3CT-23OR1304051

ORNL/TM-2023/2999

Advanced Materials and Manufacturing Technologies

PRELIMINARY FEASIBILITY OF PRINTING, MICROSTRUCTURE ANALYSIS AND MECHANICAL PERFORMANCE OF A DOWN SELECTED NI ALLOY

Sebastien Dryepondt
Stephen Taller
Fred List
Zachary Snow

July 2023

M3CT-23OR1304051

Prepared by
OAK RIDGE NATIONAL LABORATORY
Oak Ridge, TN 37831
managed by
UT-BATTELLE LLC
for the
US DEPARTMENT OF ENERGY
under contract DE-AC05-00OR22725

CONTENTS

ACRONYMS

AM	Additive Manufacturing
AMMT	Advanced Materials and Manufacturing Technologies
ANL	Argonne National Laboratory
ASME	American Society of Mechanical Engineers
BD	Build Direction
BPVC	Boiler and Pressure Vessel Code
BSE-SEM	Backscattered Scanning Electron Microscopy
BWR	Boiling Water Reactor
CCD	Central Composite Design
CT	Computed Tomography
DED	Directed Energy Deposition
EBM	Electron Beam Melting
EDS	Energy-Dispersive X-ray Spectroscopy
GE	General Electric
GFR	Gas-cooled Fast Reactor
HIP	hot isostatic pressing
HFIR	High Flux Isotope Reactor
INL	Idaho National Laboratory
LMP	Larson Miller Parameter
LPBF	Laser Powder Bed Fusion
MDF	Manufacturing Demonstration Facility
MSR	Molten Salt Reactor
NDE	Non-Destructive Examination
NE	Nuclear Energy
ORNL	Oak Ridge National Laboratory
PAC	Powder Alloy Corporation
PNNL	Pacific Northwest National Laboratory
PWR	Pressurized Water Reactor
TCR	Transformational Challenge Reactor
TEM	Transmission Electron Microscopy
VHTR	Very High Temperature Reactor

FIGURES

TABLES

ABSTRACT

This report is submitted as completion of a Milestone 3 deliverable under work package ORNL CT-23OR1304051 in support of the Advanced Materials and Manufacturing Technologies (AMMT) program. The AMMT program is aiming at the faster incorporation of new materials and manufacturing technologies into complex nuclear-related systems. An integrated approach, combining advanced characterization, high-throughput and accelerated testing, modeling and simulation including machine learning and artificial intelligence will be employed. While 316H (Fe-16-18Cr-10-14Ni-2-3Mo-0.04-0.1C) has been identified as a key alloy to be integrated into the AMMT accelerated alloy qualification approach due its relevance for many current and future nuclear energy reactors, many other alloys could be considered for the advanced fabrication of innovate high-performance nuclear components. ANL, INL, ORNL and PNNL are collaborating on identifying the most promising alloy candidates relevant for the AMMT program. A selection criteria matrix was established to evaluate the alloys considering their relative importance and technological readiness levels for nuclear energy applications, with a focus on laser powder bed fusion (LPBF). Due to the broad range of potential candidate alloys, ORNL and INL focused on Ni-based alloys, while ANL and PNNL mainly evaluated Fe-based alloys. PNNL previously published materials scorecards reports on several key alloys and this report is providing a broader overview of Ni-based candidate alloys, expending beyond alloys well-known to the nuclear community. Of particular interest are alloys that are currently commercially available in powder form due to the growing demand from other industries that have invested heavily in additive manufacturing. Among these alloys, Haynes 282 (Fe-20Cr-20Co-8Mo) was selected due to its superior strength at high temperature compared to the code-qualified alloy 617 (Ni-20-24Cr-10-15Co-8-10Mo). To assess the integration of this new alloy into the AMMT digital manufacturing framework, we performed the rapid optimization of alloy 282 printing parameters on a Renishaw 250 machine, the fabrication of sufficient materials for extensive characterization and mechanical testing both at ORNL and INL, and added the printing data into the digital platform via the Peregrine software. A detailed analysis of the LPBF 718 alloy was also conducted, with creep specimens being tested at 600-650°C and characterized by advanced electron microscopy. The alloy superior mechanical strength and great printability associated with the extensive database that has already been generated highlight the promising potential of LPBF 718 as a candidate alloy for the AMMT program. INL, ANL and PNNL have generated similar reports and all the information will be compiled into a final M2 milestone report to provide the AMMT leadership team with clear recommendations on the down selection of reactor materials, as well as establish a roadmap for the qualification of these selected alloys.

1. Introduction

Additive or advanced manufacturing (AM) allows for the fabrication of complex near net-shape components reducing the needs for machining, welding and brazing [1]. Recent studies predict that large adoption of AM will drastically impact the supply chain and global economy across multiple commercial sectors [2]. For the nuclear industry, the Transformational Challenge Reactor (TCR) program demonstrated that AM combined with artificial intelligence (AI) can deliver enabling technologies for advanced reactors [3]. Digital manufacturing is of particular relevance, utilizing the tremendous amount of information generated during printing to accelerate part qualification through analysis by advanced data analytics techniques [4-6]. Three programs across the Department of Energy (DOE) – Office of Nuclear Energy (NE) were therefore combined in FY22 to create the Advanced Materials and Manufacturing Technologies (AMMT) program aiming at developing advanced materials and processes for current and advanced nuclear technologies. As stated in the AMMT program roadmap [7], a key goal of the program is the faster incorporation of new materials and manufacturing technologies into complex

products and systems. While the core efforts of the AMMT program aim to demonstrate the potential of AM using stainless steel 316H, many other structural materials may be relevant to the program. Thus, four "Prioritization of Current Reactor Materials for Advanced Manufacturing" work packages at Oak Ridge National Laboratory (ORNL), Idaho National Laboratory (INL), Pacific Northwest National Laboratory (PNNL) and Argonne National Laboratory (ANL) aim at selecting current AM materials based on their relative importance among the candidate nuclear materials and their technological readiness levels for NE applications. This effort is a continuation of the work initiated at PNNL with the publication of a materials scorecards report ranking several relevant structural NE materials [8]. A key goal for the four laboratories was to establish a decision criteria matrix for a fair and consistent assessment of several potential structural candidate materials. Due to the large number of alloys of interest, it was agreed that ORNL and INL would focus on Ni-based alloys, while ANL and PNNL would investigate Fe-based alloys. This report summarizes both activities performed in collaboration with the other national laboratories and specific activities at ORNL and INL focused on Ni-based alloys. Similar reports were generated by the partnering national laboratories, and all the results and findings will be integrating into a final M2 milestone report, providing detailed recommendations on a few high-potential alloys to be integrated under the AMMT program.

2. Decision Criteria Matrix

The determination of relevant criteria for the selection of reactor materials to be produced by AM for NE applications is needed to ensure a consistent and transparent decision process. Materials scorecards were developed and reported by PNNL for the following nuclear-relevant materials, 316SS, 304SS, Alloy 800H, Graphite C/C, Alloy N, Silicon Carbide, HT9, Alloy 617, and Alloy 718 [8], with detailed justifications of the proposed readiness levels. The scorecards were based on published literature data, industry response to a survey, stakeholder input collected at workshops, and expert opinion. Six key categories were considered when evaluating each material: Code Availability, Gaps in Data Availability for Performance Values and Measurements, Technical Maturity for End Use/Development Stage, Deployment Readiness Requirements, Supply Chain Availability and Programmatic Factors. While significant variability in data and knowledge gaps were recognized, 316 and 304 stainless steels obtained the highest ranking being the most common stainless steels in the nuclear industry and a variant of 316 stainless steel with higher carbon content, 316H, became the focus of the AMMT program. To refine the approach and take advantage of the broad expertise at the four participating national laboratories, recurrent meetings were organized to discuss, select, and rank a broad range of relevant criteria for reactor materials selection. The current decision criteria matrix is shown in Table 1 with 6 key categories and 34 individual criteria. The initial matrix was presented at several review meetings and at an industrial workshop at ORNL and modified based on participants' feedback. This matrix is expected to evolve with time based on constant feedback from main stakeholders. The definition and relevance of each individual criteria will be provided in the final collaborative report and information on each category of the decision criteria matrix is provided in this report.

Category	Criteria					
Manufacturing/Powder	Powder Availability	Powder Properties	Powder Chemistry	Cost	Recycling	
Manufacturing/Components	Printability (LBF)	Defects	Post Treatment	Processing Window	Weldability	Surface Roughness Surface Finish
History & Applications	NE Experience	Other Industries Experience	Data Availability	Code Data Availability	Experience With Non-LPBF AM	Scaling Up
Mechanical Properties	Creep	Fatigue	Creep-Fatigue	High Temp Tensile Strength	Room Temp	
Environmental Effects	Radiation Resistance	Oxidation Resistance	Stress Corrosion Cracking	Molten Salt	Liquid Metal	
Physical Properties	Thermal Properties	Solidification-Relevant Properties	Other modeling-relevant properties	CT-Relevant Properties		
Microstructure	Material Homogeneity	Microstructure Stability	LPBF Microstructure Specificity			

Table 1*:* Decision criteria matrix that will guide the selection of materials to be evaluated under the AMMT program.

2.1 Manufacturing / Powder

This category is focused on powder production, with a key parameter being powder availability. A limited number of powders are commercially available, and the production of custom-made powders often requires large quantities (>500lbs) of expensive powders to be ordered, with 2-3 month delivery times. During the AMMT industrial workshop hosted at the Manufacturing Demonstration Facility (MDF) at ORNL in May 2023, many industrial partners expressed their concerns with the existing AM feedstock supply chains. Other significant parameters to be considered are the powder chemistry, often based on specifications for wrought or cast alloys, the powder cost and quality, and the number of times the powder can be reused.

2.2 Manufacturing / Components

While the powder category focuses on what is added to the AM process, this category addresses the fabrication of industrial components. The printing window resulting in parts with low defect density needs to be identified. Post fabrication treatment, mainly heat treatments and/or hot isostatic pressing (HIP), will drastically impact the component microstructure, performance and cost. Surface roughness and/or surface finishing will affect component properties such as fatigue resistance, corrosion, or fluid dynamics. The difficulty in using conventional non-destructive examination (NDE) techniques on as printed AM components with rough surface finish was also highlighted during the AMMT industrial workshop. While AM allows for the fabrication of complex components, welding to other structures might be required and the weldability of the alloy after AM needs to be assessed.

2.3 History and Applications

The interest in a material for one of the current or future nuclear power reactors is a major consideration as highlighted in the AMMT roadmap [7] and materials scorecards report [8]. Experience from other industries contribute to the history of an alloy and may also be critical as AM is more heavily employed by other sectors such as aerospace and land-based gas turbines industries. This also means that data relevant to the NE industry, in particular mechanical properties, might already exist with some of the data being relevant to code qualification in the American Society of Mechanical Engineers (ASME) Boiler and Pressure Vessel Code (BPVC). While the AMMT program is currently focused on laser

powder bed fusion (LPBF) as a fabrication method, the fabrication of material/components using other AM techniques such as directed energy deposition (DED), electron beam welding (EBM), binder jetting, and wire-based AM might be relevant when considering speeding up fabrication time and the fabrication of large components.

2.4 Mechanical Properties

The relevant mechanical properties for components durability will vary from one reactor concept to another but the requirements for ASME BPVC code qualification are well known with the key properties being tensile, creep, fatigue and creep-fatigue at relevant temperatures.

2.5 Environmental Effects

The relative radiation resistance and the influence of radiation on property evolution will be needed for any type of reactors, and such data will only be generated by the nuclear community. On the contrary, material compatibility with the working fluid will be highly dependent on the reactor concept, and relevant corrosion data needs to be generated in very specific environments such as liquid metal (Na, Pb) or molten salt (Fluoride or Chloride), For these reactor concepts, these data are crucial as material compatibility is clearly one of the major limiting factors. For current reactor systems, data on stress corrosion cracking are the most needed. As with mechanical performance, data generated on material compatibility in other industries will be assessed.

2.6 Physical Properties

During printing, melting and solidification of the alloy will be dependent on the material's thermal and physical properties. Data are, therefore, required to develop microstructure predictive models and establish correlation between microstructure and properties. In-situ and ex-situ detection of defects is a key objective of the AMMT digital manufacturing approach, and physical properties impacting both in-situ imaging and NDE characterization need to be considered.

2.7 Microstructure

Materials produced by additive manufacturing are known to be heterogeneous at different length scales and a current AMMT work package is assessing the impact of 316H microstructure inhomogeneity on its performance. Rapid solidification and high cooling rates also lead to non-equilibrium microstructure. The stability of the microstructure at the expected use temperatures and stresses needs to be considered for ASME BPVC qualification and during material selection. Microstructure similarities between AM and wrought or cast alloys might accelerate alloy qualification, since extensive database often exist for the wrought version of the AM alloy.

3. Evaluation of Ni-based Alloys

Ni-based alloys are prime candidates for NE components due to their superior high temperature strength and oxidation resistance. Several extensive reviews of Ni-based alloys in use or considered for nuclear applications have already been published [9-12]. The previous PNNL materials scorecards report focused on four Ni-based alloys well-known to the nuclear community, 800H, 718, 617 and Alloy N. This report evaluates three categories of Ni-based candidate alloys for the AMMT program: low Co alloys, high temperature high strength alloys and low Cr molten salt compatible alloys. The LPBF 718 and LPBF 282 alloys have been the focus of this report, and ongoing work on the fabrication and characterization of these two alloys is discussed.

3.1 Low Co Ni-based Alloys

Low Co Ni-based alloys can be considered for components closer to the core outlet, experiencing significant neutron fluxes. The three key alloys to be evaluated in this category are alloy 718, 625 and 800H, but only the 718 and 800H alloys will be discussed in this report. Information on alloy 625 can be found in the companion report prepared by INL.

3.1.1 Alloy 718

3.1.1.1 718 current status

Superalloy 718 is one of the most used Ni-based superalloys with many applications for aircraft and land-based gas turbine engines [13]. The exceptional strength of the alloy at temperature up to ~700°C is due to the presence of strengthening nano-size γ' and γ'' precipitates. While developing the Ni-based 625 alloy, Special Metals researchers observed a drastic improvement of the yield strength of Ni-based alloys due to the addition of Nb and Mo, which led to the discovery of 718 [14]. Alloy 718 is currently used in Boiling Water Reactor (BWR) and Pressurized Water Reactor (PWR) and advanced reactor designs such as the Gas-cooled Fast Reactor (GFR) and the Very High Temperature Reactor (VHTR) are looking into the potential use of alloy 718 components for high temperature applications [8-9]. As the "workhorse" alloy for the gas turbines and aerospace industries, companies such as Siemens Energy and General Electric (GE) have acquired extensive experience in fabricating 718 components by additive manufacturing. As an indication of Siemens's involvement in the AM-production of 718, Siemens and Senvol recently advertised a partnership to commercialize databases for three AM-produced alloys, Ni-based 718, Ni-based 625 and Ti-based Ti64 [15]. A broad range of component demonstration projects involving AM 718 have been reported by GE, from a partnership with Shell to produce an oxygen hydrogen micromixer [16] to the large-scale fabrication of an Advanced Additive Integrated Turbine Centre Frame (TCF) 718 casing [17]. On the nuclear side, Inconel 718 was a candidate alloy for several structural elements below the reactor core [18].

Such an interest in AM 718 components has led to the development of a reliable supply chain, with 718 powder being commercially available from many powder manufacturers, including Praxair, Carpenter, Oerlikon, Powder Alloy Corporation (PAC), etc. It is worth noting that on the Praxair powder website, only two powders have dedicated powder datasheets, Ni-based 718 and Ni-based 625 [19], while Carpenter highlights only three Ni-based alloys on its website, alloy 718, alloy 625 and Hastelloy X [20]. Requirements for the 718 powder manufacturing, thermal processing, microstructure, properties, etc., are covered by the ASTM F3055-14a, "Standard Specification for Additive Manufacturing Nickel Alloy (UNS N07718) with Powder Bed Fusion".

In addition to the substantial experience from industry, extensive literature has been published on AM 718. In their review article on AM Ni-based alloys in 2021, Sanchez et al. estimated that 192 studies out of 290 were focused on alloy 718 (68%) [21]. Hot cracking is often considered as the main challenge for Ni-based superalloy printing and is directly related to the γ' volume fraction, and thus the Al and Ti concentration [22]. With its very low Al and Ti contents, alloy 718 is considered as a printable superalloy with the only potential defect being porosity, which can be minimized, and a density superior to 99.9% in the as printed conditions is achievable [23]. Tensile data generated at both room and high temperature on as printed LPBF 718 showed variations of properties based on the specimen orientation, with higher strength but lower ductility perpendicular to the build direction. Columnar grains along the build direction with a cellular structure or fine dendrites have been reported for the as printed material, explaining the observed anisotropic tensile behavior for the as printed LPBF 718. In addition, the presence of laves and δ phases in the as printed conditions has a deleterious impact on the alloy tensile properties [24-26]. Many authors have, therefore, studied the effect of heat treatments and/or HIP'ing on the alloy microstructure and performance [25-28]. As expected, the microstructure and in particular the volume fraction of δ phase is strongly impacted by the solution annealing temperature [29] but Taller and Austin [27] showed that

tensile properties at 20-600°C superior or similar to the properties of wrought 718 can be achieved after the following HT2 heat treatment: homogenization at 1174 °C for 2h and 1204 °C for 6h, solution anneal at 1093 °C for 1h and aging at 718 °C and 621 °C, both for 8h. These excellent tensile properties were due to a recrystallized grain structure, high fraction of γ" precipitates and a low fraction of intragranular δ-phase. In addition to tensile data, two research teams studied the impact of the microstructure, surface finish and heat treatment on the LPBF 718 fatigue performance [28, 32]. Komarasamy et al. [28] reported number of cycles to failure similar to wrought 718, both in the as printed and annealed conditions, and they concluded that the high-volume fraction of δ phase at grain boundaries did not impact significantly the alloy fatigue behavior. Kevinsanny et al. performed fatigue testing on HIP'ed and annealed LPBF 718 specimens, with or without surface polishing, and concluded that the rough surface of the AM specimen did not decrease the alloy fatigue performance due to the presence of large equi-axed grains [32].

Moreover, Sanchez et al. performed creep testing at 650°C, 600MPa, on 718 material fabricated by LPBF using one or several lasers [33]. Specimens were then machined at 0°, 45°and 90° with respect to the build direction. All the specimens were heat treated according to the AMS 5662 standard i.e. 980 °C/1 h/gas quench, 720 °C/8 h/furnace cooling to 620 °C/8 h/gas quench. They observed longer lifetimes for the specimens machined along the build direction, with the multi-laser strategy resulting in lifetimes similar to the lifetimes measured for wrought 718. All the specimens exhibited, however, a very low ductility at rupture, again with superior results along the build direction with a deformation at rupture of ~7%, but still significantly lower than the 29% average strain measured for the wrought 718 creep specimens. It is, however, worth noting that a deformation of ~30% for wrought 718 is quite high and might not be representative of a fully heat treated wrought 718 [34]. Brinkman et al. analyzed creep data from several 718 heats and showed that the ductility decreases with the increase of the creep lifetime [35].

Kuo et al. [36] studied the effect of build direction and heat treatment on the creep properties of direct metal laser sintering and observed better performance along the build direction. However, in all cases, very low creep lifetime and elongation at rupture were observed for the AM material in comparison with wrought 718 (strain at rupture of 7%). They concluded that the inferior AM creep properties were due to δ precipitates in the interdendritic region and the presence of a cellular structure with high dislocation density. The amount of δ phase decreased with increasing the solution anneal temperature, with nearly complete disappearance of the δ phase at T>1120°C, but increasing the temperature also resulted in grain growth and carbide formation at grain boundaries [37]. HIP'ing improved the creep lifetime but did not enhance creep ductility at rupture, with all the AM specimens exhibiting less than 2% deformation at rupture. Wu et al. [38] conducted similar creep experiments at 650°C, 650MPa after different heat treatments and they drew the same conclusions i.e. lower lifetime and ductility for the LPBF 718 compared to wrought 718. They attributed the lower creep lifetime in the as printed condition to the presence of deleterious δ and Laves phases at grain boundaries leading to grain boundary cavitation and cracking. Due to the elongated grain structure along the build direction, this degradation mechanism also explains the lower lifetimes measured perpendicular to the build direction.

Finally, it was reported in the PNNL materials scorecards report that no irradiation study has been published on the LPBF 718 alloy [8], but Taller and al. recently submitted an AMMT milestone report on the evolution of LPBF 718 after irradiation at ORNL's High Flux Isotope Reactor (HFIR) [18]. The heat treated LPBF 718 showed negligible differences to the yield strength and ultimate tensile strength at both 300°C and 600°C with an irradiation of 2dpa.

3.1.1.2 Ongoing 718 evaluation

As mentioned previously, limited creep studies have been published on LPBF 718, all reporting lower lifetime and lower ductility compared to wrought 718. The use of LPBF materials previously fabricated under the TCR program was a great opportunity to initiate creep testing on material with a well-known pedigree [18, 27]. Since the material exhibited excellent tensile properties after the HT2 heat treatment described above, it was decided to assess the material creep properties both in the as printed and

after exposure to HT2. A Concept X-Line 2000R machine at the Manufacturing Demonstration Facility (MDF) was used to fabricate a large block, and the powder chemistry provided by the supplier was Ni-18.22Fe-19Cr-5.15Nb-0.93Ti-0.5Al-0.04Si-0.04C-0.0012N-0.016O in wt%. The large block was sectioned into four identical pieces with nominal dimensions of 59mm×18mm×15mm, one of which was heat treated according to HT2.

Prior to creep testing, microstructural evaluation was performed at the grain level and lower length scales. Standard metallographic grinding using successively finer grits of SiC paper and polishing using diamond solutions with successively decreasing particle sizes of 6 μm, 3 μm, and 0.25 μm were performed until a mirror-like surface was achieved with ~0.02 μm silica particles. Surface characterization was performed on a Tescan MIRA3 GHM scanning electron microscope (SEM) using 20 keV electrons. Electron backscatter diffraction (EBSD) Kikuchi band patterns were collected on an Oxford Instruments Symmetry EBSD detector with AZtec software using a step size of 1 μm. At each point, the AZtec software indexes the Kikuchi band structure and determines the Euler angles of the lattice. The open source MTEX toolbox [40] was used to generate orientation maps and inverse pole figures and to determine grain sizes from the Euler angles exported from AZtec for grains consisting of more than 5 pixels. The equivalent grain diameter was calculated by taking the area of the two-dimensional grain determined by the orientation map, A, and assuming a circular area through Eq. (1) and the degree of sphericity was calculated from this diameter, the grain boundary area, and the length of the grain perimeter, P, through Eq. (2). The sphericity, Ψ, ranges from 0.5 being a perfect circle to 0 being a straight line.

$$d_{eq} = 2\sqrt{\frac{A}{\pi}} \tag{1}$$

$$\Psi = \frac{A}{\frac{1}{2}d_{eq} * P} \tag{2}$$

Microstructure characterization occurred at regions nearest to the gauge region of the SS3-type dog bone specimens and consisted of backscattered scanning electron microscopy (BSE-SEM) with electron backscatter diffraction (EBSD) to quantify grain size and morphology. An example of the length scales of investigation can be seen in Figure 1 for the as printed LPBF 718. Even with the minimal contrast from typical BSE-SEM imaging, a columnar grain structure is visible, oriented along the build direction. This texture became apparent in the EBSD grain orientation maps, shown in Figure 2 with the corresponding sphericity. Many grains in the as printed LPBF alloy 718 displayed an [001] orientation, or near there, and elongated preferentially in the build direction. This is evident in the sphericity where larger grains display a lower degree of sphericity. Within the grains, the color intensities corresponding to grain orientation are not uniform, suggesting a degree of residual stress internal to the grains causing minor variations in crystal structure. The observations in the as printed LPBF alloy 718 are in stark contrast to the HT2 condition in which the grains are much larger with uniform orientations within each grain. Transmission electron microscopy (TEM) revealed the presence of a high density of γ" in HT2 [27]. TEM of as printed alloy 718 is on-going to determine the nanoscale microstructure and assess heterogeneities such as a dislocation cell structure that may influence the creep behavior.

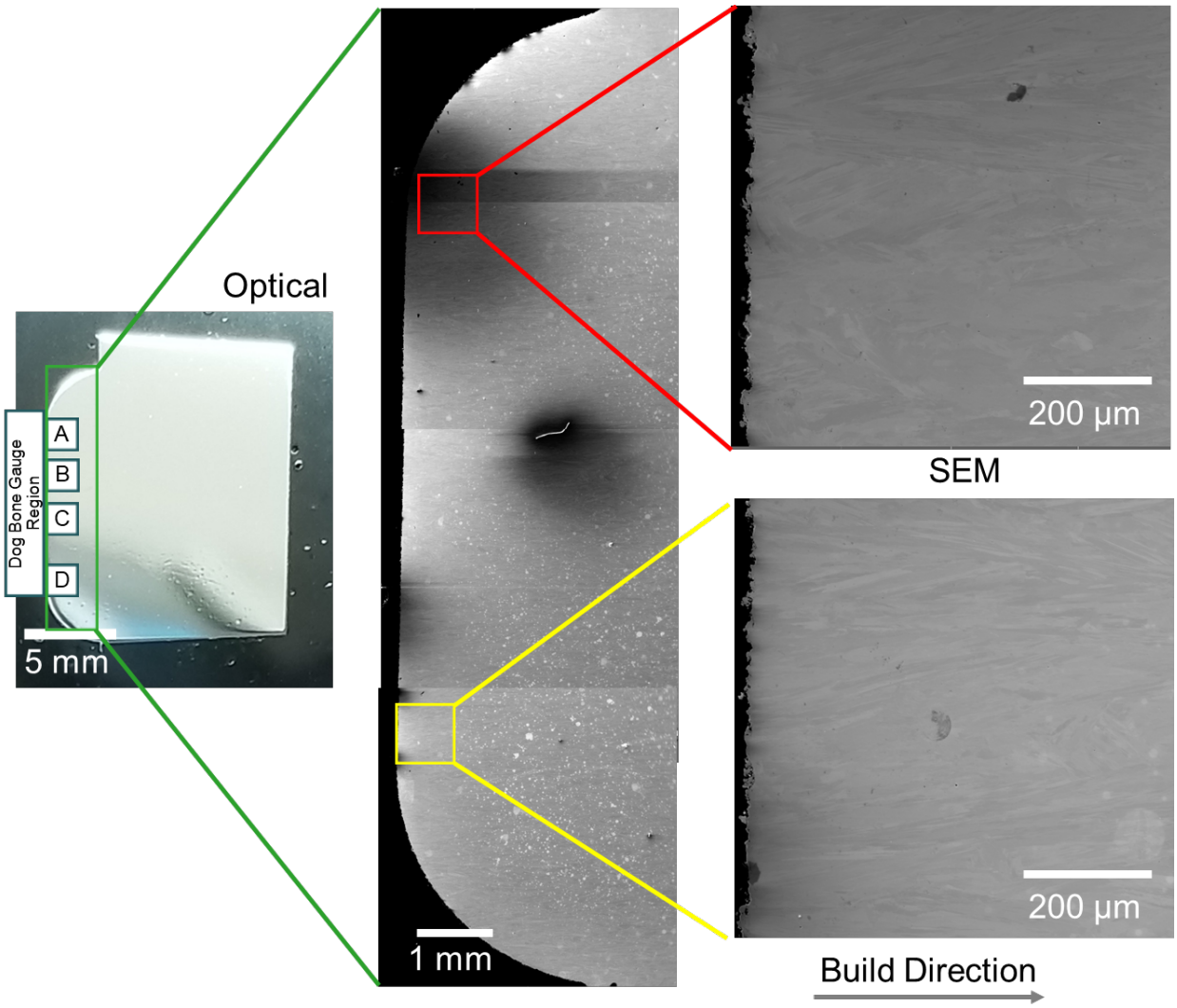

Figure 1: Overview of the microstructure characterization across length scales for as printed superalloy 718 near the gauge region of a creep dog bone.

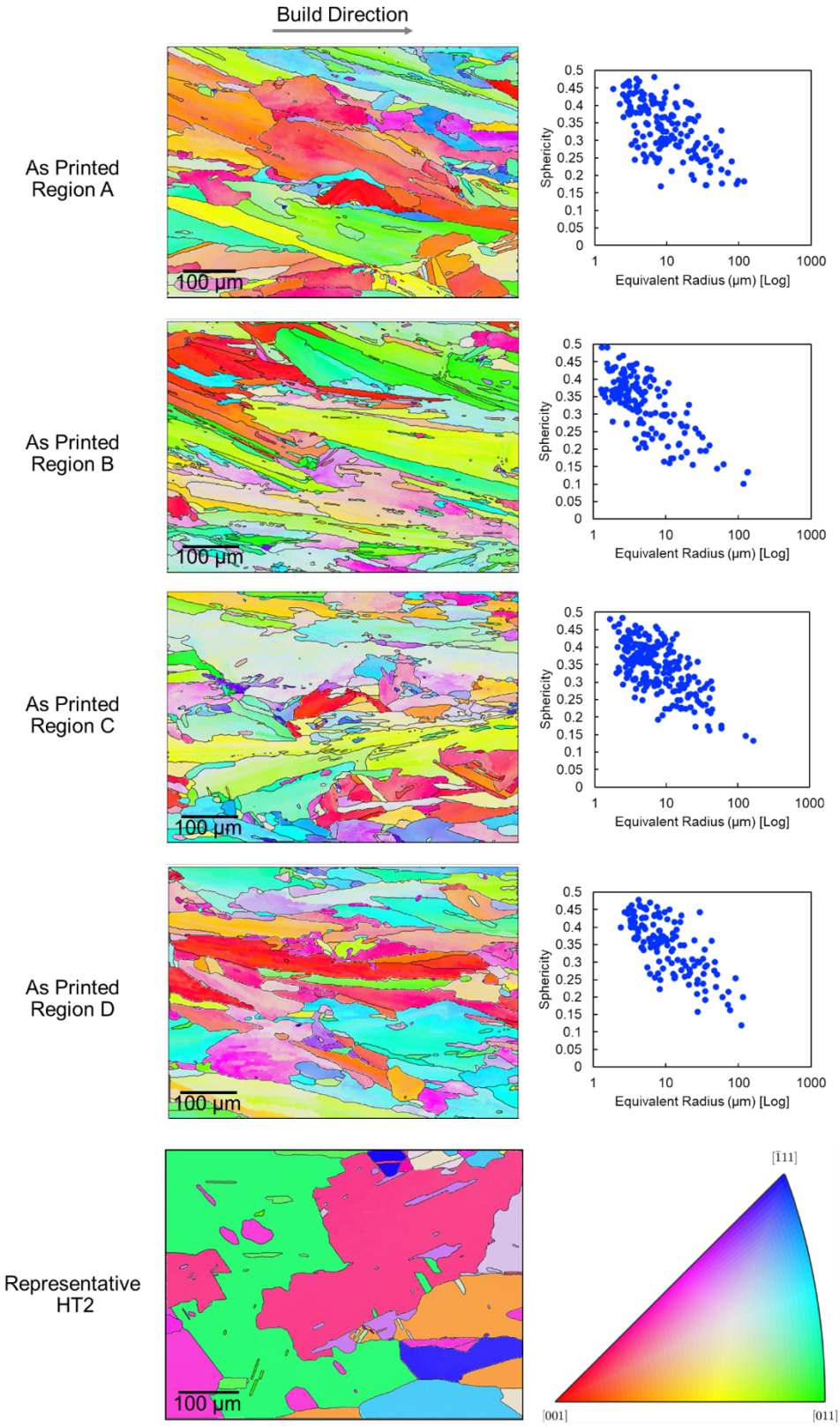

Figure 2: EBSD orientation maps for as printed LPBF alloy 718 with regions corresponding to those identified in Figure 1 with corresponding measures of grain sphericity and a representative EBSD grain orientation map for HT2.

For creep testing, SS3-type dog bone specimens with a gage length of 7.62 mm and a gage section of 1mm × 2 mm were machined along and perpendicular to the build direction from an as printed ~9 mm × 29 mm×15 mm LPBF 718 rectangular block, as seen in Figure 3. Specimens were also machined along the build direction from the block annealed according to HT2 and all the specimens were polished using a 600 grit sandpaper before creep testing. Testing was then conducted on dead-load frames equipped with a radiation furnace using custom made high temperature grips for shoulder loading. Rods clamped to the top and bottom grips were connected to two Linear Variable Differential Transformers (LVDT) to generate semi quantitative creep curves. Two thermocouples were attached to the specimens and the temperature was controlled within +-2 °C of the target temperature. Creep testing was conducted at 600 °C, with an applied stress of 750 MPa and at 650 °C with an applied stress of 600 MPa or 650 MPa.

Generated creep curves are shown in Figure 4 and the creep results are summarized in Table 2. As reported in the literature, most of the specimens exhibited low ductility, with a 2 to 5% ductility at rupture except for one HT2 specimen with a ductility of 9.5%. The creep lifetimes were slightly superior for the HT2 specimens compared to the as printed specimens, and the lifetime was marginally higher along the build direction in the as printed condition. These results are compared in the Larson Miller plot presented in Figure 5 with creep data for wrought 718 from Haynes International and LPBF 718 literature data [33, 36-38]. The Larson Miller Parameter (LMP) was calculated according to the relation:

$$LMP = T(°K) * \left(C + \log\left(t_r(h)\right)\right), with\ C = 20 \quad (3)$$

With T, temperature in ° K and t_r, time to rupture in h.

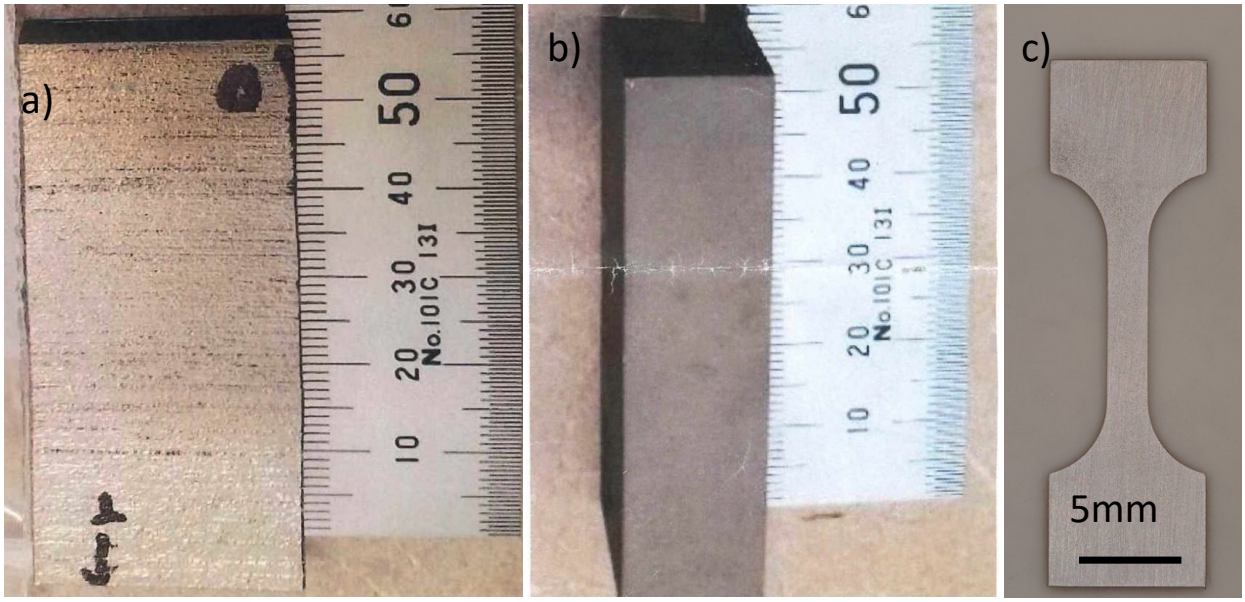

Figure 3: a) LPBF 718 block used to machine the as printed specimens along and perpendicular to the build direction, b) Block used to machine the annealed specimens along the build direction, c) Example of one annealed specimen before testing.

The specimen lifetimes are overall consistent with expected lifetimes for wrought 718 and superior to the lifetimes reported in the literature for LPBF 718. The low deformations at rupture are also consistent with reported results for LPBF 718 [33,36-38]. Significant data scattering is expected for the deformation at rupture for wrought 718 [35] but ductility at rupture lower than ~2% for LPBF 718 might be a concern for NE structural applications.

Specimen	Condition	Orientation	Temp. (°C)	Stress (MPa)	lifetime (h)	LMP
9VS1	As Fabricated	BD	650	650	385	20850
9VS6	As Fabricated	BD	600	750	724	19960
9HS3	As Fabricated	Per. To BD	650	650	357	20819
9HS6	As Fabricated	Per. To BD	600	750	524	19837
92S1	HT2	BD	650	650	18	19622
92S3	HT2	BD	650	650	463	20924
92S6	HT2	BD	600	750	991	20079
92S4	HT2	BD	650	600	536	20982

Table 2: Summary of the creep tests conducted on as printed and annealed LPBF 718. BD = Build Direction. Per. = perpendicular

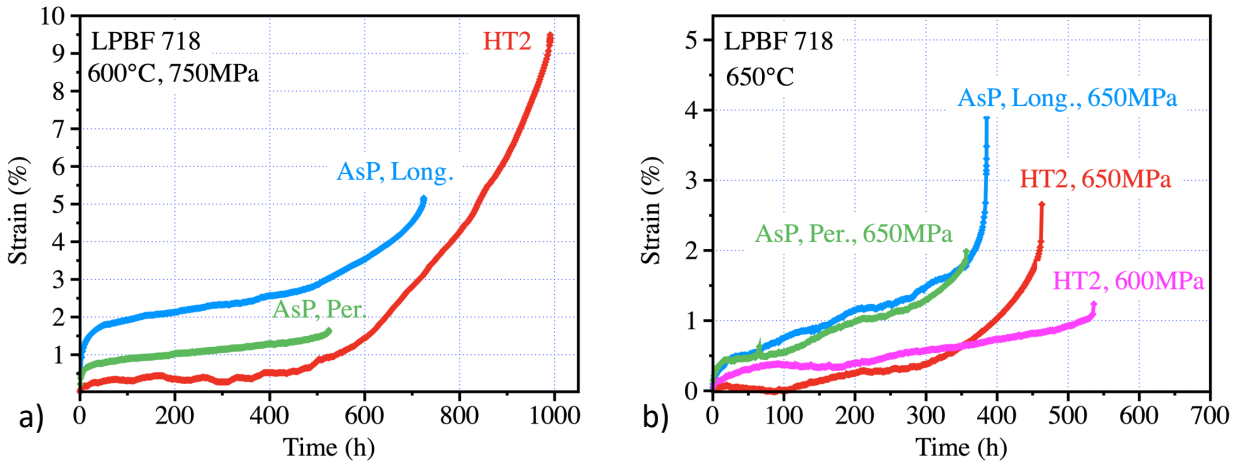

Figure 4: LPBF 718 creep curves for the as printed and annealed specimens, a) 600 °C, 750 MPa, b) 650 °C, 600 MPa or 650 MPa. AsP. stands for As printed, Per. for perpendicular to the BD and Long. for along the BD.

The ruptured specimens were then cross-sectioned and polished using standard metallographic techniques as described previously. BSE-SEM micrographs are shown in Figure 6 for the specimen tested at 650 °C, 650 MPa in the as printed condition and tested along the build direction. Only a few cracks were observed and as shown in Figure 6b, these cracks were related to voids formation at grain boundaries. As can be seen in Figure 6b-6c, the initial cellular structure was still present after 385h at 650 °C, with elongated cells ~1 µm in size. Figure 6c also highlights locally the formation of a dendritic structure rather than a cell structure with significant chemical segregation, as illustrated by the Nb energy-dispersive X-ray spectroscopy (EDS) map in Figure 6d.

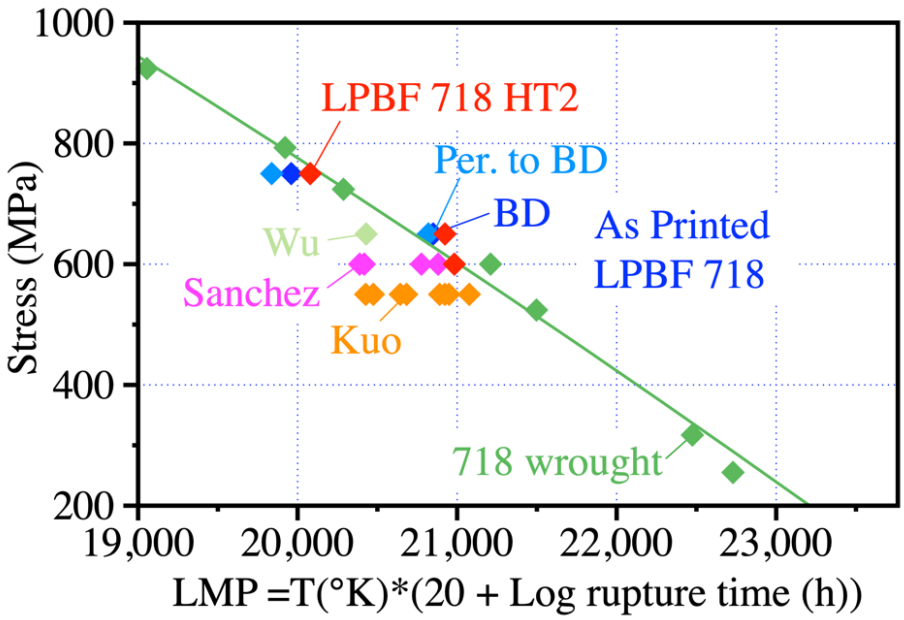

Figure 5: Comparison in a Larson Miller plot of the creep performance of the LPBF 718 alloy with wrought 718 according to Haynes datasheet and LPBF 718 literature data [33,36-38].

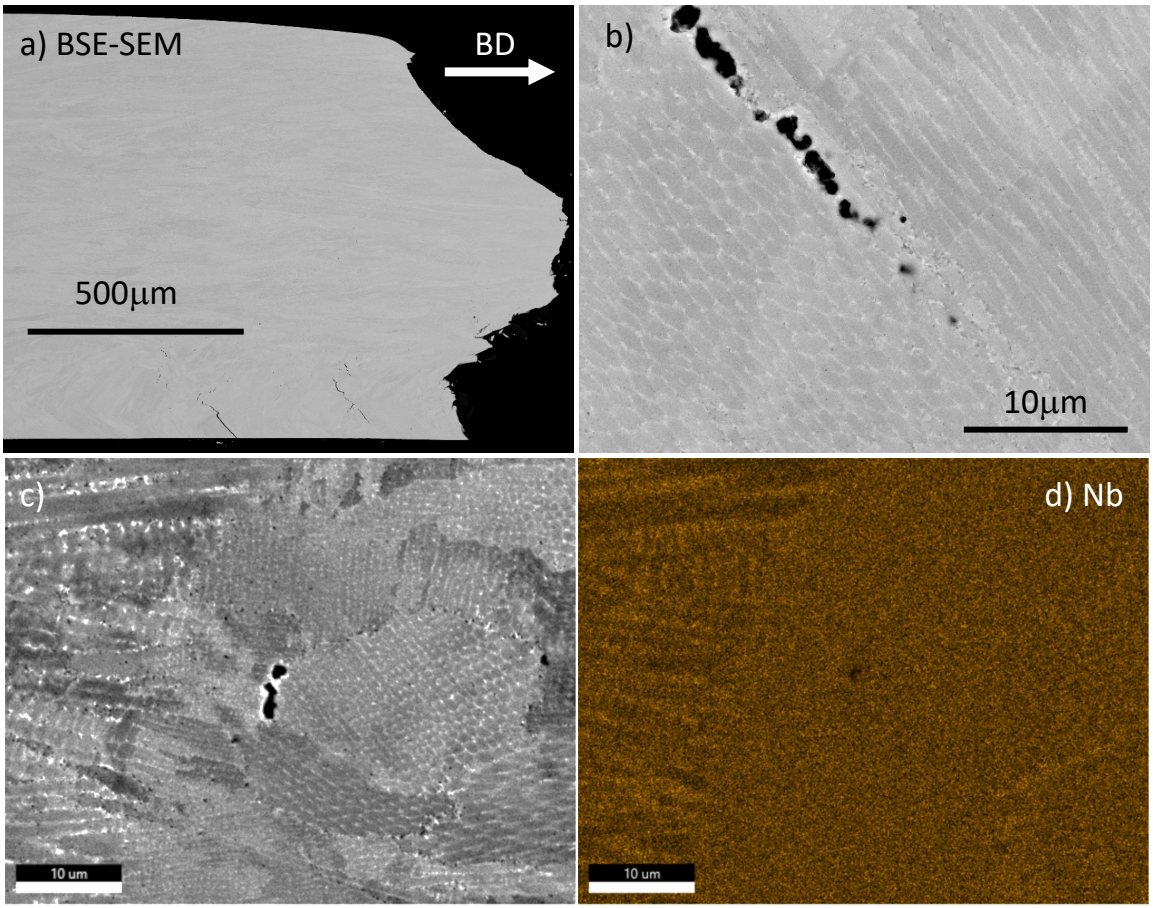

Figure 6: BSE-SEM cross-section micrographs of the as printed specimen machined along the build direction after creep testing at 650 °C, 650 MPa for 385h.

As can be seen in Figure 7, similar microstructural features were observed for the as printed specimens tested at 650 °C, 650 MPa perpendicular to the build direction. Voids and cracks were again observed mainly at grain boundaries with the clear presence of a cellular structure. The EDS elemental maps in Figure 8 revealed the segregation of Mo and Nb at the cellular structure level. While segregation of Ti was not clearly observed, several authors have reported the formation of (Mo, Nb)-rich Laves phases in the walls of the LPBF 718 cellular structure [28,36-37]. Figure 8a revealed that similar precipitates have formed at grain boundaries, with also the presence of Cr-rich precipitates.

As can be seen in Figure 9, the microstructure was very different for the HT2 specimen creep tested at 650 °C, 650 MPa for 463h. As described in [18,27] and shown in Figure 2, the HT2 heat treatment resulted in the formation of equi-axed grains and the disappearance of the cell structure, consistent with Figure 9b and 9c. Cracking was again observed only at grain boundaries, with the presence of coarse precipitates, identified in Figure 10 as (Nb,Ti)-rich carbides. The higher magnification micrograph in Figure 9d highlights the presence of the nano-size strengthening γ' and γ" precipitates, but transmission electron microscopy (TEM) is needed for in-depth characterization of these precipitates.

The microstructure for the as printed longitudinal specimen tested at 600° C, 750 MPa was very similar to the microstructure at 650 °C and is not reported here. On the contrary, the microstructure for the heat-treated HT2 specimen tested at 600 °C, 750 MPa was quite different compared to the microstructure observed at 650 °C and BSE-SEM micrographs are shown in Figure 11. Cracking was, as always, observed at grain boundaries but needle-like precipitates, likely δ phase, were observed all over the specimen. These δ precipitates made it more difficult to image the nano γ' and γ" precipitates but Figure 11d clearly reveals the presence of these precipitates. EBSD and TEM will be conducted to clearly identify and quantify all the precipitates in these creep-tested specimens. While the characterization of the post-creep microstructure is in progress, the strong agreement between the LPBF 718, with or without HT2, and the wrought 718 on the Larson-Miller plot suggests the strong differences in initial grain structure, and the nanoscale dislocation cell structure, are not the primary influence on creep performance, and precipitating phases may be the dominant microstructure feature.

In addition, while the creep lifetime presented here are superior to what has been reported in the literature for LPBF 718, likely due to the specific HT2 heat treatment, including homogenization at 1174°C and 1204°C, further improvement in creep ductility might be needed for NE applications. In collaboration with other high temperature alloy programs, additional 718 material will be printed and annealed to further improve our understanding of the process-microstructure-creep properties relationship at 550-700° C.

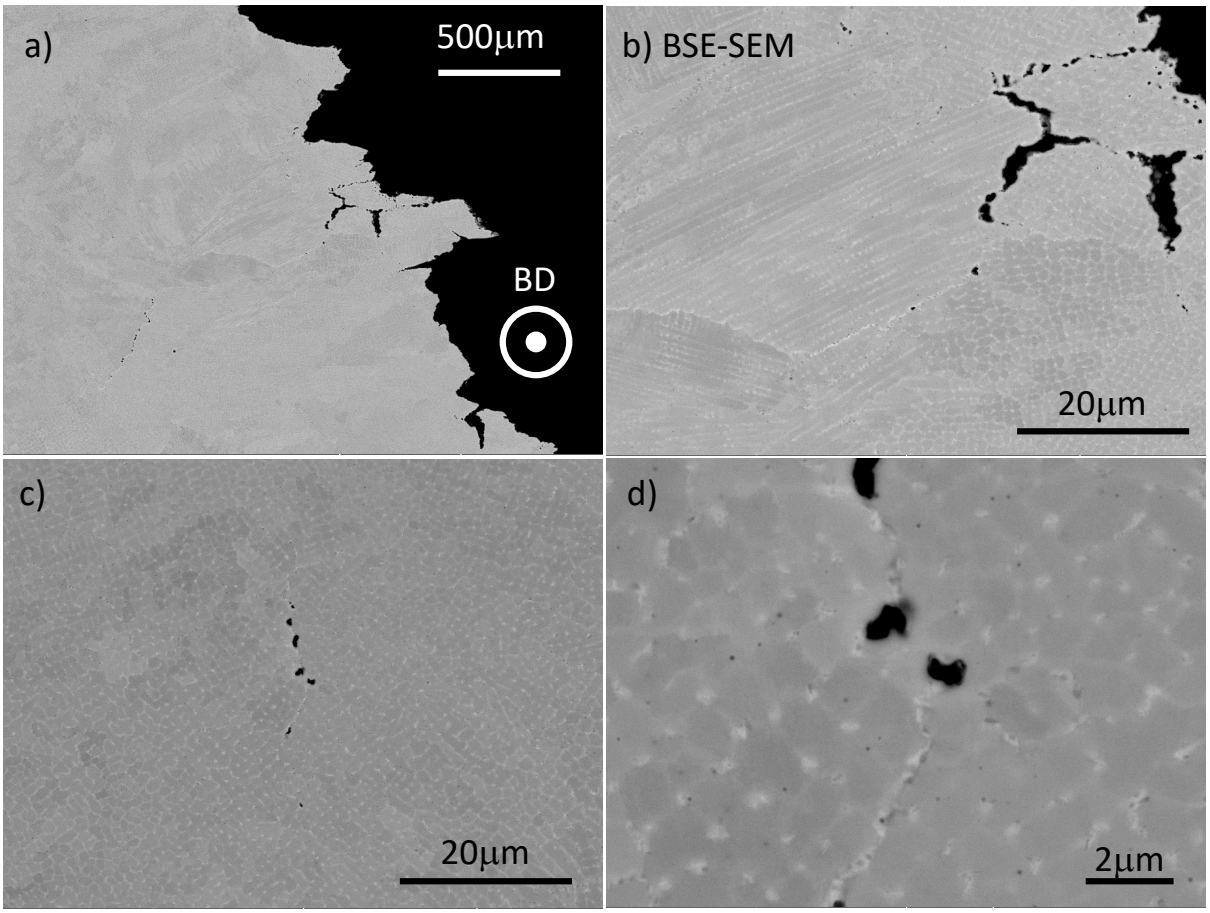

Figure 7*:* BSE-SEM cross section micrographs of the as printed specimen machined perpendicular to the build direction after creep testing at 650 °C, 650 MPa for 357h.

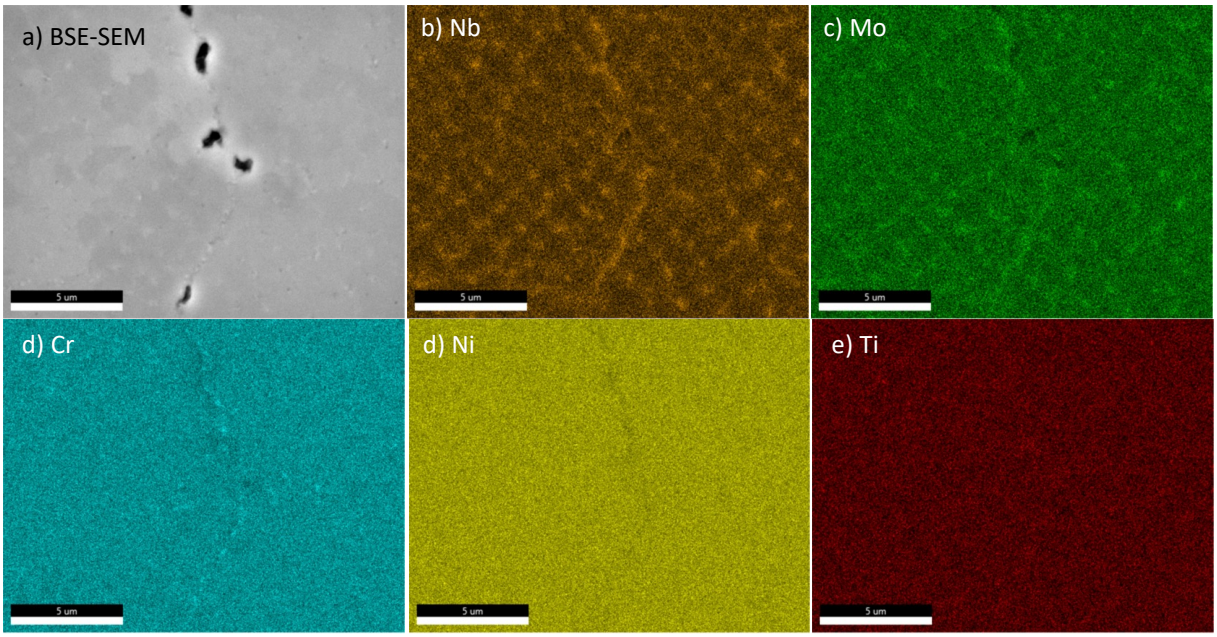

Figure 8 : a) BSE-SEM micrograph of the as printed specimen machined perpendicular to the build direction after creep testing at 650 °C, 650 MPa for 357h, b)-e) Corresponding EDS elemental maps.

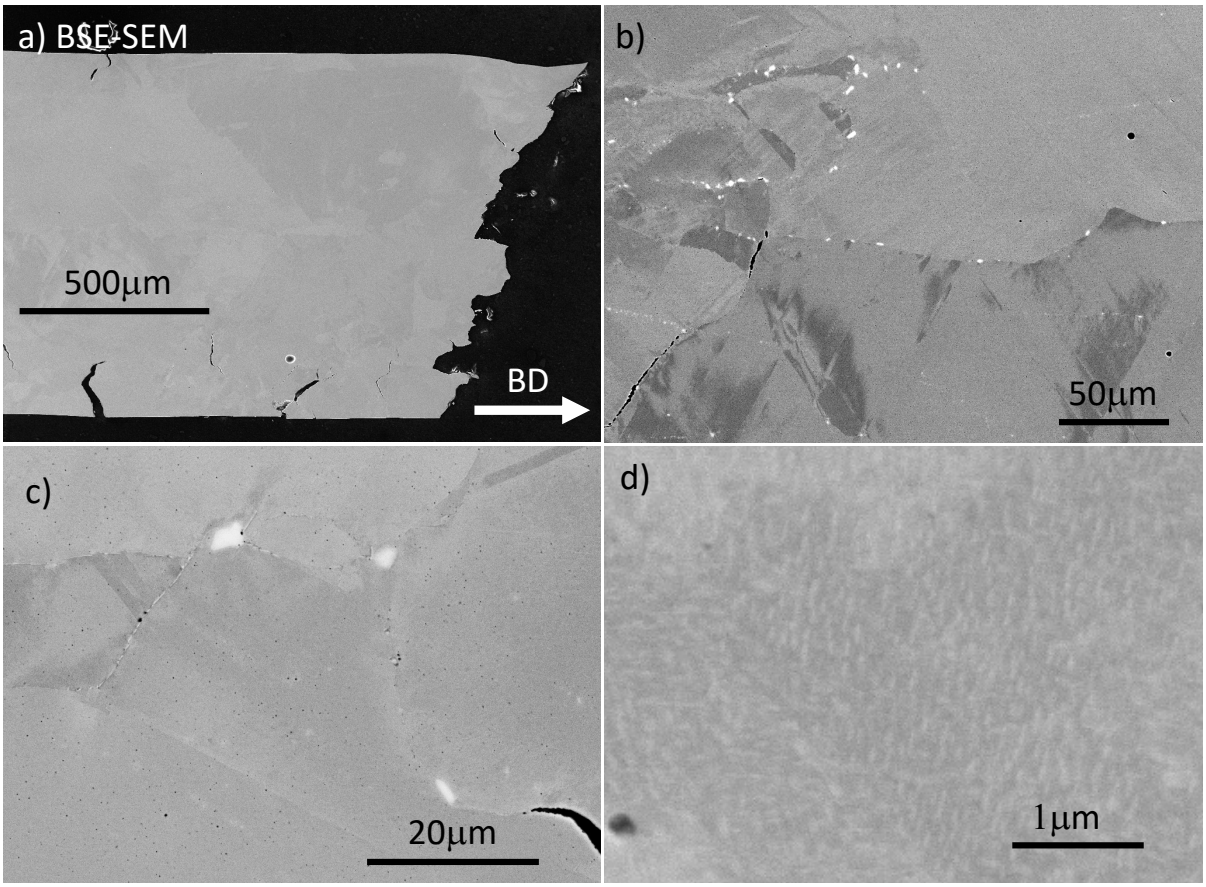

Figure 9: a) BSE-SEM cross-section micrographs of the annealed specimen machined along the build direction after creep testing at 650°C, 650MPa for 463h.

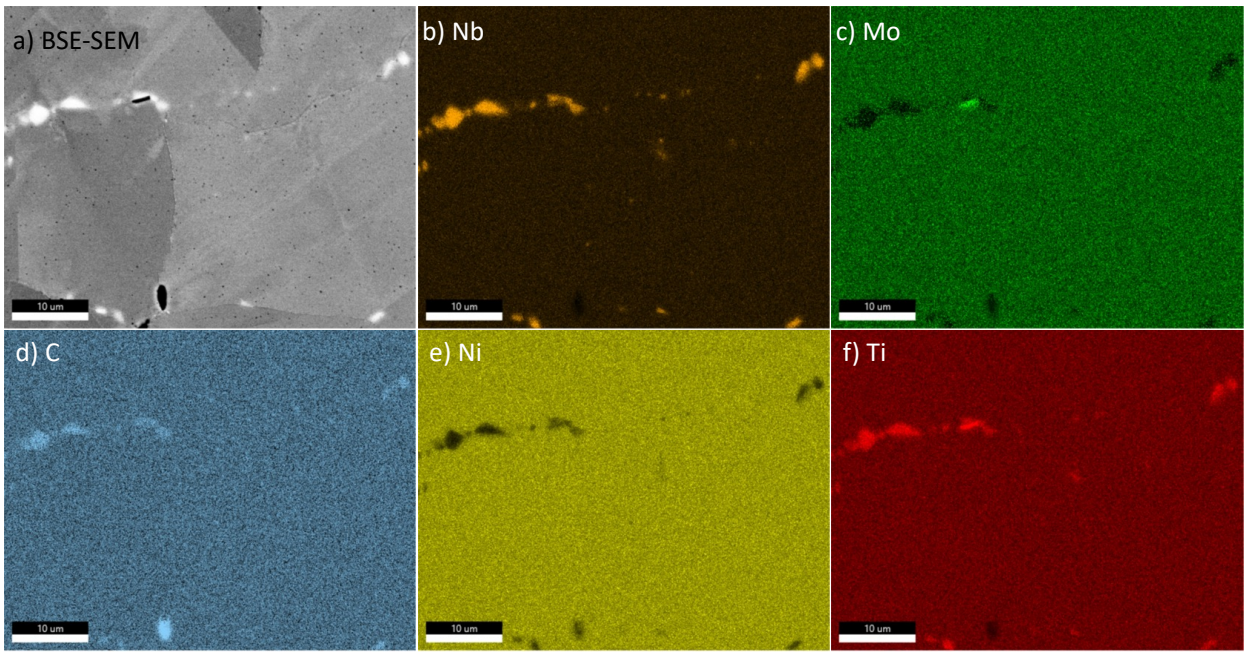

Figure 10: a) BSE-SEM cross section micrograph of the annealed specimen machined along the build direction after creep testing at 650°C, 650MPa, b)-e) Corresponding EDS elemental maps.

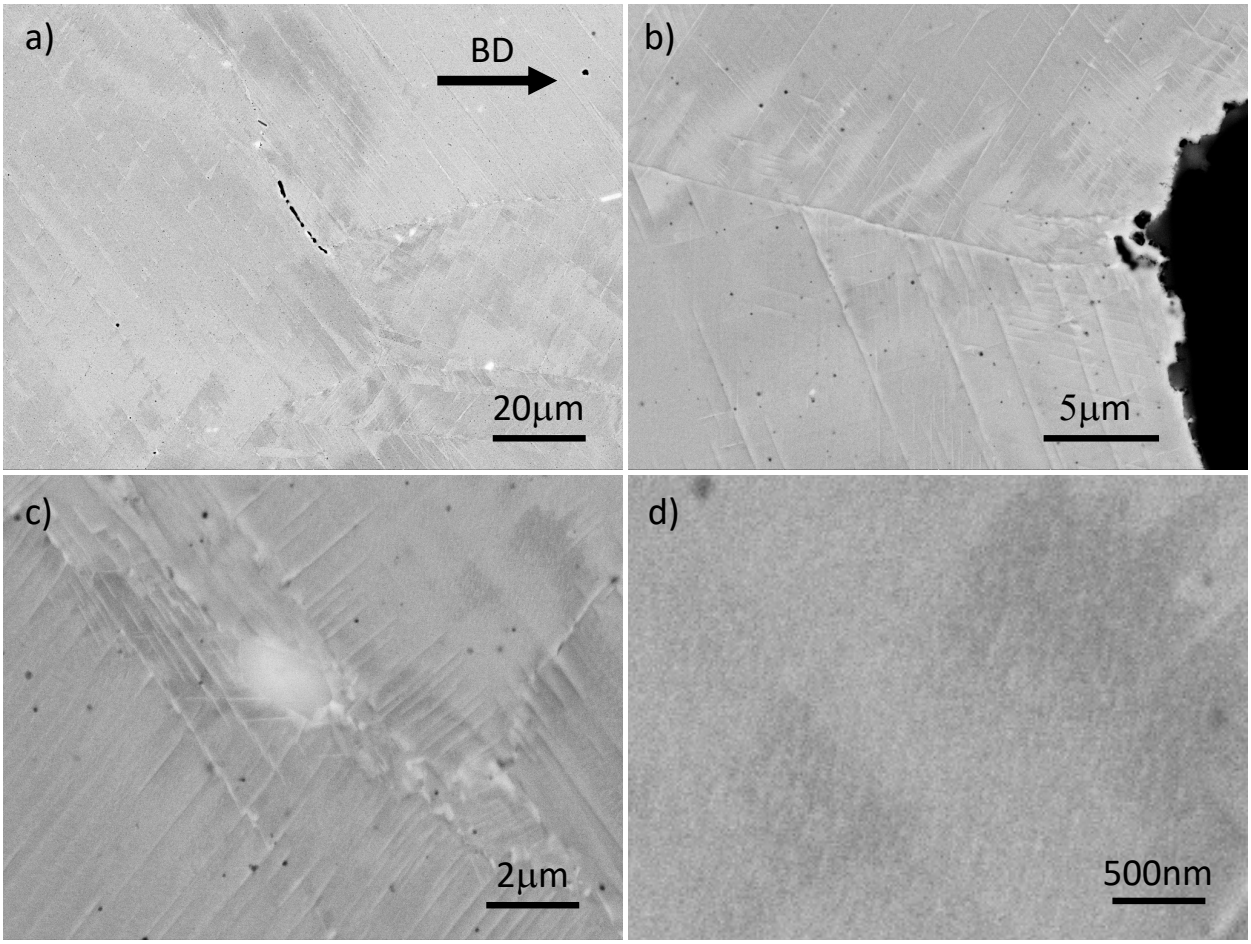

Figure 11: a) BSE-SEM cross section micrographs of the annealed specimen after creep testing at 600°C, 750MPa.

3.1.1.3 718 ranking

In the PNNL materials scorecards report, alloy 718 received a score of 4 for "Programmatic Factors" due to the use of the alloy in current reactors and the potential use in GFR and VHTR advanced reactors, and a score of 3 was attributed to the alloy for supply chain availability. Looking at the selection matrix criteria presented in Table 1, alloy 718 will score well in the powder and component manufacturing categories since high quality 718 powder is routinely produced by several powder manufacturers, and complex components are already being produced for a broad range of applications. Knowledge of the LPBF 718 extends way beyond the NE industry, with tremendous experience from the aerospace and gas turbines industries. This report focused on LPBF 718, but it is worth noting that alloy 718 has been produced using a broad range of AM techniques, including EBM [41], DED [42], wire-based large-scale AM [43] and binder jetting [44]. Code data availability is certainly the limiting factor in the "History & Applications" category. Mechanical properties data is already available but published data on creep, fatigue and creep-fatigue is limited. A significant amount of data has likely been generated by industry, but these results have not been shared. Partnership with key industrial partners such as Siemens or GE could give the AMMT program access to these data. Our current work also shows that the AMMT program could rapidly generate relevant data to improve the LPBF 718 scorecard. The microstructure of the LPBF alloy has been extensively characterized in the as printed conditions and after various heat

treatments, but the long-term stability, with and without stress, needs to be studied further. This is also the case for information related to environmental effects. Corrosion and/or stress corrosion data for the LPBF 718 are currently missing, but the AMMT program is in a good position to generate such data and compare the results with wrought 718. This was accomplished in FY22 and FY23 on the irradiation side, with the generation of unique data at HFIR at 300°C and 600°C.
Finally, the physical properties required for microstructure prediction during printing e.g. thermal properties, phase diagrams, etc. are already available and have been utilized by several teams to correlate processing parameters with microstructure. The aerospace industry is also heavily invested in digital manufacturing, and alloy 718 has been integrated in approach similar, but not as advanced, as the AMMT approach using the Peregrine software.

3.1.2 Alloy 800H

Alloy 800H (Fe-30-35Ni-19-23Cr-0.05-0.1C) was discussed extensively in the PNNL materials scorecards report. A high "Programmatic Factors" score was given to the alloy due to its potential use in nuclear reactor designs such as Molten Salt Reactor (MSR) and VHTR. It was, however, noted that very little is known of the alloy fabricated by AM, with only two papers by Yang et al. investigating the sensitization and stress corrosion cracking performance of LPBF 800H in the as printed and annealed conditions [45,46]. The report mentioned that 800H powder can be ordered from Carpenter Powder Products, but the company was contacted and has stopped producing the alloy. A powder quantity of >~500lbs would need to be ordered for Carpenter to consider producing the alloy. A detailed evaluation of the LPBF 800H will be provided in the next report, but the alloy readiness score will be low due to lack on information on AM 800H and limited powder availability.

3.2 High Temperature High Strength Alloys

These high temperature alloys offer much high temperature capability compared to austenitic steels but cannot be considered for applications in the vicinity of the reactor core due to their high Co content. While 617, is an obvious candidate alloy as the only Ni-based alloy code-qualified, other alloys of interest will be discussed, in particular Haynes 282, due to their superior high temperature performance. Additional high temperature Ni-based alloys are also discussed in the INL companion report.

3.2.1 Alloy 617

Alloy 617 (Ni-20-24Cr-10-15Co-8-10Mo-0.65-1.15Ti-0.8-1.5Al-0.05-0.15C) was discussed in detail in the PNNL materials scorecards report [8]. The attractiveness of alloy 617 comes mainly from the alloy code qualification in 2019 for construction of nuclear components in ASME BPVC section III. As a solution strengthened alloy with temperature of use up to 950°C, alloy 617 is considered for VHTR designs. The alloy high strength is also of interest for MSRs but the high Cr content limits the alloy compatibility with chloride and fluoride salts. The drawbacks of alloy 617 are the lack of powder availability and the limited number of studies published to date on AM-617. While 617 powder is not currently a commercial product, ordering 617 powder from Praxair is occasionally possible based on other customers' requests, and 90lbs of 617 will be acquired August 2023 to assess the alloy printability. To our knowledge, only two papers have been published on the fabrication and characterization of alloy 617 by AM, and in both cases, the alloy was fabricated by wire-based AM [47-48].

3.2.2 Alloy 282

3.2.2.1 282 current status

Haynes 282 (Ni-20Cr-10Vo-8.5Mo-2.1Ti-1.5Al) is a γ'-strengthened superalloy developed by Haynes International for high temperature structural applications, especially for the aerospace and land-based gas turbines industries [49]. The 282 alloy was identified as a potential candidate for Advanced Ultra-Supercritical (A-USC) components such as steam turbine disk (wrought) or turbine valve body (cast) which led to an extensive study of the alloy creep, fatigue and creep fatigue performance [50-52]. The ASME Boiler and Pressure Vessel Code Case 3024 was approved in 2021 for alloy 282 [53]. The LMP plot in Figure 12 compares the performance of the alloy 282 with other Ni-based alloys, in particular alloy 617 [54]. A significant improvement in creep performance is observed when compared with alloy 617 for LMP values < ~27000, corresponding to temperatures lower than ~850°C. The volume fraction of γ' decreases significantly at temperatures >850°C leading to creep properties comparable to the creep properties of alloy 617 above this temperature. It is also worth noting that 282 exhibits a similar behavior as alloy 718 at high stresses and low temperature, but at temperatures >700°C γ' precipitates in alloy 282 are more stable than the γ" in alloy 718. Due to potential applications in SCO_2 and molten salts, the high temperature corrosion performance of alloy 282 has been evaluated in various environments [55-57].

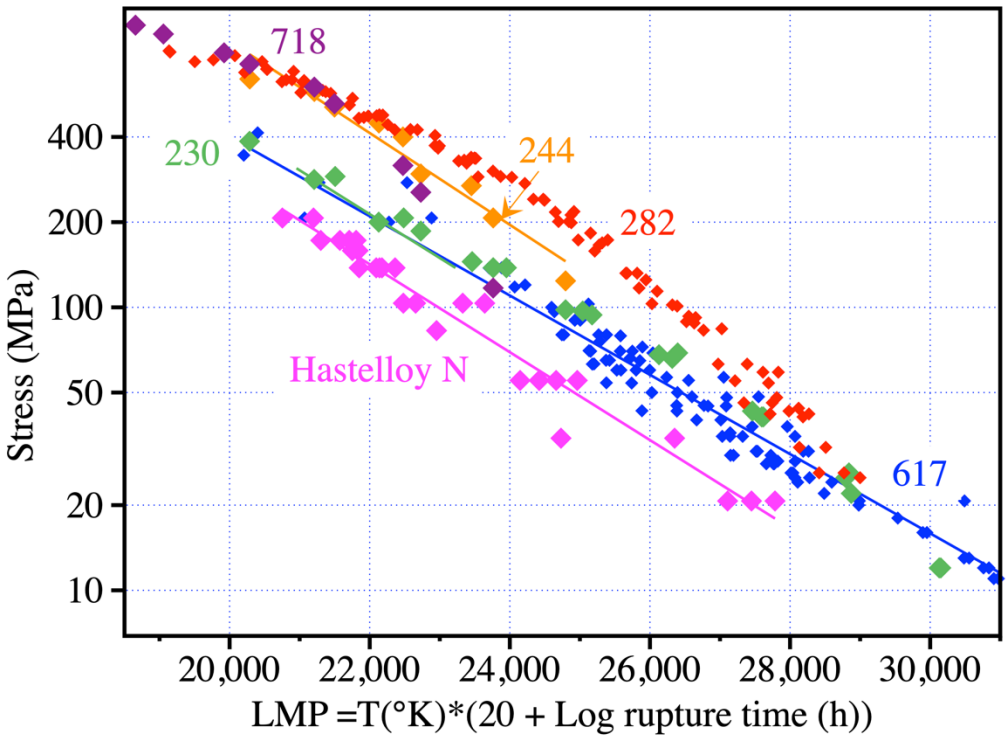

Figure 12: Comparison of the creep properties of alloy 617, 282, 230, Hastelloy N and 244 using an LMP plot.

A key goal when developing alloy 282 was to balance the alloy strength and fabricability by carefully controlling the Ti and Al contents to achieve a γ' volume fraction of ~20% [49]. This relatively low volume fraction of strengthening γ' for a superalloy is also limiting / suppressing hot cracking during AM printing, which explains the growing interest for the alloy from the LPBF community and gas turbine industry. Crack-free high density LPBF 282 has been fabricated, and the as-printed microstructure

consisted of textured grains elongated along the build direction, with also the presence of a cellular structure [58-60]. Slightly lower yield and ultimate tensile strength and higher ductility have been reported for the as printed LPBF 282 in comparison with wrought 282, with higher strength but lower ductility perpendicular to the build direction [59]. After conducting a full heat treatment with a solution annealing at 1150°C for 1h and the standard double-aging treatment, 2h at 1010°C followed by 8h at 788°C, the situation was reversed, with higher yield and ultimate tensile strength for the annealed LPBF 282 compared to wrought 282, but lower ductility. Shaikh et al. also measured tensile properties at 800°C and reported similar strength for the annealed LPBF 282 and wrought 282, but higher ductility for the wrought alloy [59]. It is worth noting that the standard solution annealing at 1150°C for 1h did not result in the alloy recrystallization, as already mentioned by Christofidou et al. [61]. To achieve recrystallization, Boswell et al. annealed the LPBF 282 alloy for 1h at 1250°C, followed by a one-step aging treatment at 788°C for 8h [60]. No fatigue data has been published to date on LPBF 282 and only a few short-term creep tests have been performed on annealed LPBF 282. Boswell et al. performed ten creep tests at 750°C, 410MPa and the ~80h lifetime was consistent with wrought 282 data [60]. Shaikh et al. carried out creep testing at 927°C, 89MPa and the lifetime was superior to the lifetime for wrought 282 along the build direction but inferior perpendicular to the build direction [59]. It is worth reminding that Boswell et al. annealed the material at 1250°C and achieved recrystallization while elongated grains along the build direction where still present after 1h at 1150°C for the LPBF 282 material creep tested by Shaihk et al.. 30nm γ' precipitates were observed by Shaihk et al., as expected from the standard single or double aging heat treatments for alloy 282 [62], but Boswell et al. observed larger non spheroidal γ' precipitates due to a slow cooling rate after the solution annealing treatment. Finally, as expected, no data is currently available on the alloy performance under irradiation.
Haynes 282 powder is a commercial product proposed by several key powder manufacturers, including Praxair, Oerlikon, Hogonas, PAC and key AM machine manufacturers such as Renishaw and EOS can provide recommended printing parameters for the alloy. A few research projects are exploring the use of LPBF 282 for the fabrication of high temperature SCO_2 heat exchangers [63,64] but limited information has been shared by industry on current applications.

3.2.2.2 Ongoing 282 evaluation

Alloy 282 was selected for additional evaluation due to the superior properties of the wrought alloy compared to wrought 617, promising existing data for the LPBF 282 alloy, and powder availability. In addition to generating relevant creep, fatigue and creep-fatigue data for LPBF 282, the goal is to assess integration of a new alloy into the AMMT accelerated component qualification framework. 200lbs of 282 powder was purchased from Praxair and the powder was received ~4 weeks after the purchase order was submitted. The powder chemistry provided by Praxair was as follows: Ni-19.37Cr-10.24Co-8.33Mo-2.11Ti-1.54Al-0.05C -0.03Si-0.01O in wt%. A Renishaw 250 machine was used at the MDF to optimize the 282 printing parameters and fabricate large rods and blocks for microstructure and mechanical properties characterization. The Renishaw machine was first upgraded with new cameras to generate during printing in-situ data that can be integrated into the AMMT digital manufacturing approach using the Peregrine software [65,66]. A Central Composite Design (CCD) centered on Renishaw's recommended laser parameters for alloy 282 was used to optimize the processing parameters. While the laser power and layer thickness were kept constant at 200W and 60μm, respectively, three key factors were evaluated, the hatch distance, point spacing and exposure time, resulting in the fabrication of 18 samples. A "standard Zeiss" geometry was used to be consistent with current AMMT work on 316H and facilitate both in-situ data analysis using the Peregrine software and ex-situ computed tomography (CT) scan measurements. Table 3 summarizes the printing parameters for the 18 samples and Figure 13 shows the printing configuration and the resulting Zeiss build.

Characterization of the fabricated samples included visual inspection, mass and skeletal (pycnometer) density measurements. The volumetric energy density (VED) input was also calculated according to the following relationship:

$$VED = \frac{P \cdot t}{p \cdot h \cdot l} \quad (4)$$

Where P is the laser power, t the exposure time, p the point spacing, l the layer thickness and h the hatch spacing.

Variations of the specimen mass and skeletal density as a function of the calculated VED are given in Figure 14a and Figure 14b, respectively. The sample mass increased rapidly with increasing VED to reach a plateau at ~45J/mm^3. Visual inspection revealed high level of porosity at low VED and swelling at high VED. A similar trend was observed for density measurements at VED >~42 J/mm^3, but significant results variability was observed at lower VED. A high fraction of open porosities not included into the skeletal density measurement is likely the reason for the data scattering. Based on these results, parameters corresponding to sample 13 i.e hatch spacing of 86µm, point spacing of 70µm, and exposure time of 80µs, were considered as optimum for the processing of alloy 282 and selected for the fabrication of larger builds. It is worth noting that the selected hatch spacing is not the recommended one by Renishaw, 86µm versus 100µm, but Renshaw is likely also considering the build rates, which is faster with a 100µm hatch spacing and could reduce production cost. The two large builds that were then fabricated, one for ORNL and one for INL, are displayed in Figure 15. Each of the rods and rectangular blocks were engraved to ensure the data that will be generated can be integrated into the digital manufacturing approach. The build configurations were based on the standard tensile/creep specimens at ORNL, and the standard tensile/creep and fatigue specimens at INL. As can be seen in Figure 16, the INL smooth button head fatigue specimen is 6" long, requiring, therefore, rods 6" long and 0.75" in diameter or plates 6" long and 0.75" thick. A summary of all the samples and corresponding intended use is given in Table 4. In addition to the mechanical testing samples, one rod and 4 thin plates, 0.02" to 0.08" thick, will be utilized at ORNL for microstructure characterization. While ORNL was fabricating the 282 material, INL was conducting heat treatments on LPBF 282 rods provided by EOS. Once the optimum microstructure has been achieved, samples will be heat treated and machined. Analysis of the Zeiss build by CT scans was also initiated and the higher density of the Ni-based alloy did not seem to impact defect detection. Additional information will be provided in the final report.

Sample	Hatch (µm)	Point Spacing (µm)	Exposure Time (µs)	Comments
14	90	65	60	Corner
4	110	65	60	Corner
16	90	75	60	Corner
15	110	75	60	Corner
11	90	65	100	Corner
8	110	65	100	Corner
3	90	75	100	Corner
10	110	75	100	Corner
13	86	70	80	Axial
17	114	70	80	Axial
12	100	63	80	Axial
18	100	77	80	Axial
6	100	70	52	Axial
9	100	70	108	Axial
2	100	70	80	Replicates
7	100	70	80	Replicates
5	100	70	80	Replicates
1	100	70	80	Replicates

Table 3: Summary of the LPBF 282 printing parameters for the Central Composite Design.

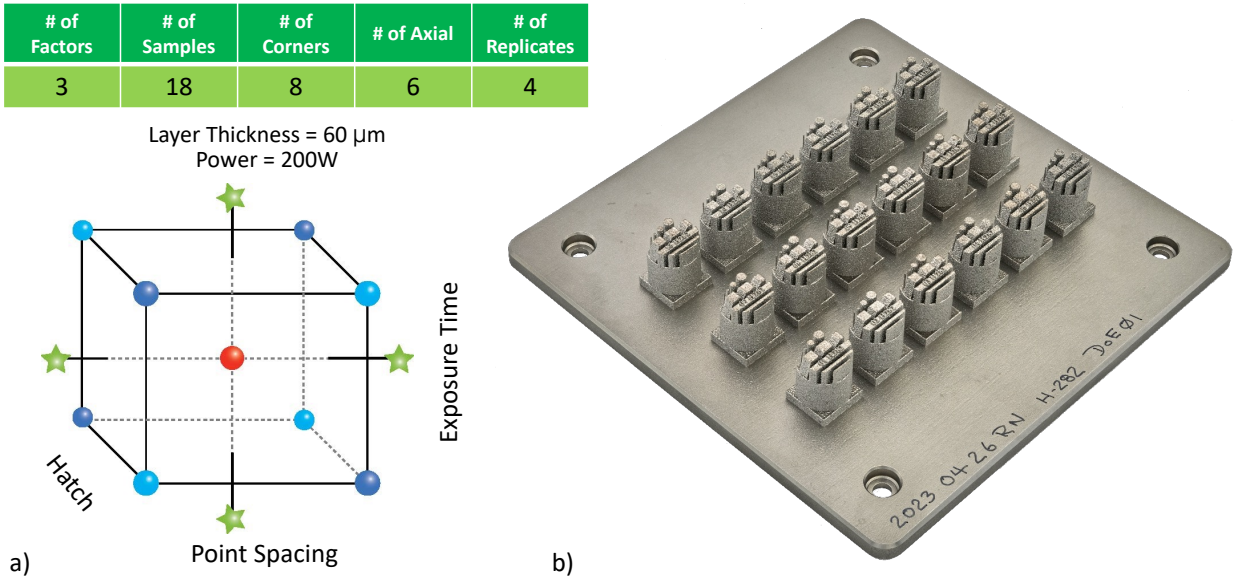

Figure 13: a) Printing configuration based on the Central Composite Design, b) resulting LPBF 282 Zeiss build.

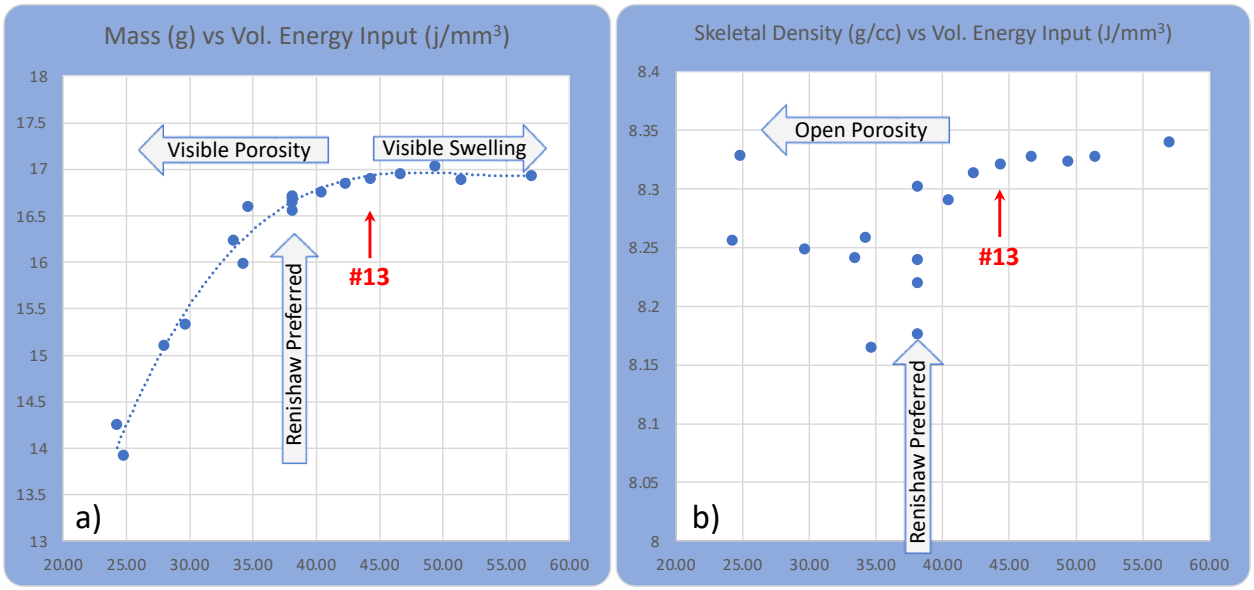

Figure 14: Characterization of the LPBF 282 samples, a) mass versus VED, b) Skeletal density versus VED.

Build	Geometry	Dimention	Number	Testing	Engraving
ORNL	Cylindrical	0.5" dia, 4" long	10	Tensile along the BD	T1 to T10
ORNL	Cylindrical	0.5" dia, 4" long	10	Creep along the BD	C1 to C10
ORNL	Cylindrical	0.5" dia, 4" long	1	Microstructure char.	MC
ORNL	Rectangular	0.5"x5"x4"	1	Tensile per. To BD	HT1 to HT7
ORNL	Rectangular	0.5"x5"x4"	1	Creep per. To BD	HC1 to HC7
ORNL	Thin plates	0.5"x4"x(0.02", 0.04", 0.06" or 0.08")	3	TBD	1 to 3
INL	Cylindrical	0.5" dia, 6" long	8	Tensile along the BD	TV1 to TV10
INL	Cylindrical	0.5" dia, 6" long	8	Creep along the BD	CV1 to CV10
INL	Cylindrical	0.75" dia, 6" long	8	Fatigue along the BD	FV1 to FV8
INL	Rectangular	0.5"x6"x4"	1	Tensile per. BD	V sign
INL	Rectangular	0.5"x6"x4"	1	Creep per. BD	V sign
INL	Rectangular	0.75"x6"x6"	1	Fatigue per. BD	V sign

Table 4: Summary of the samples fabricated for characterization and mechanical testing at ORNL and INL.

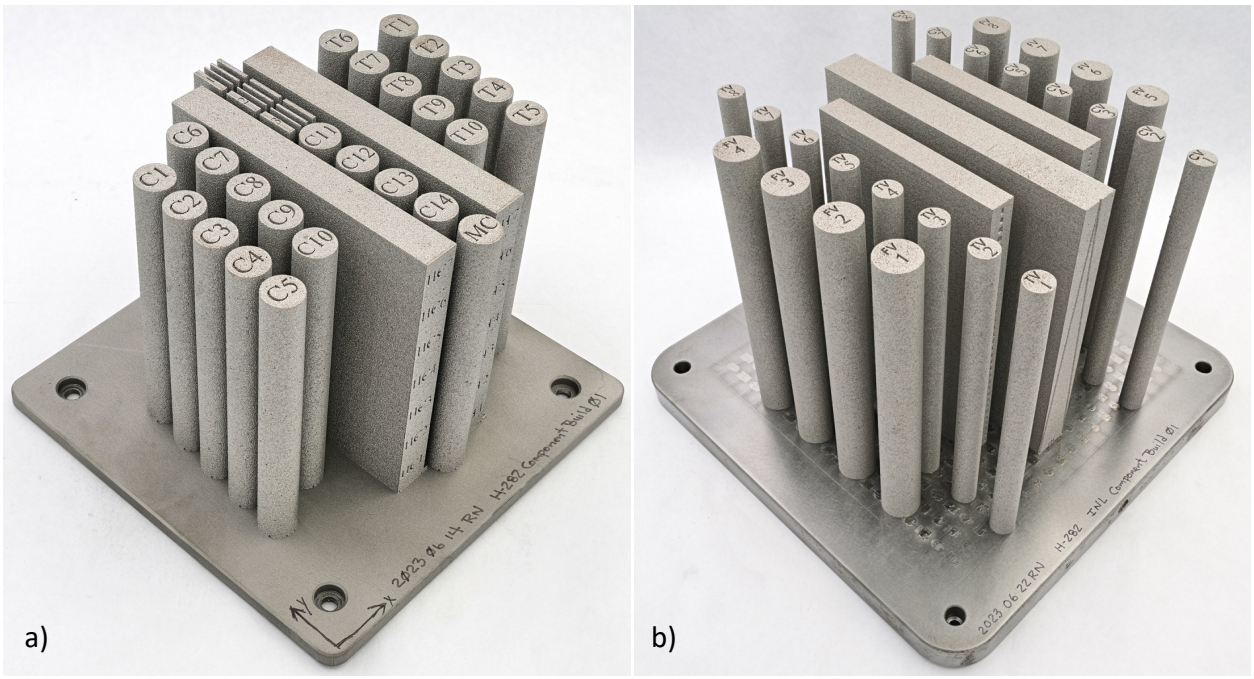

Figure 15: Large builds for mechanical testing, a) ORNL build, 4” tall and b) INL build, 6” tall.

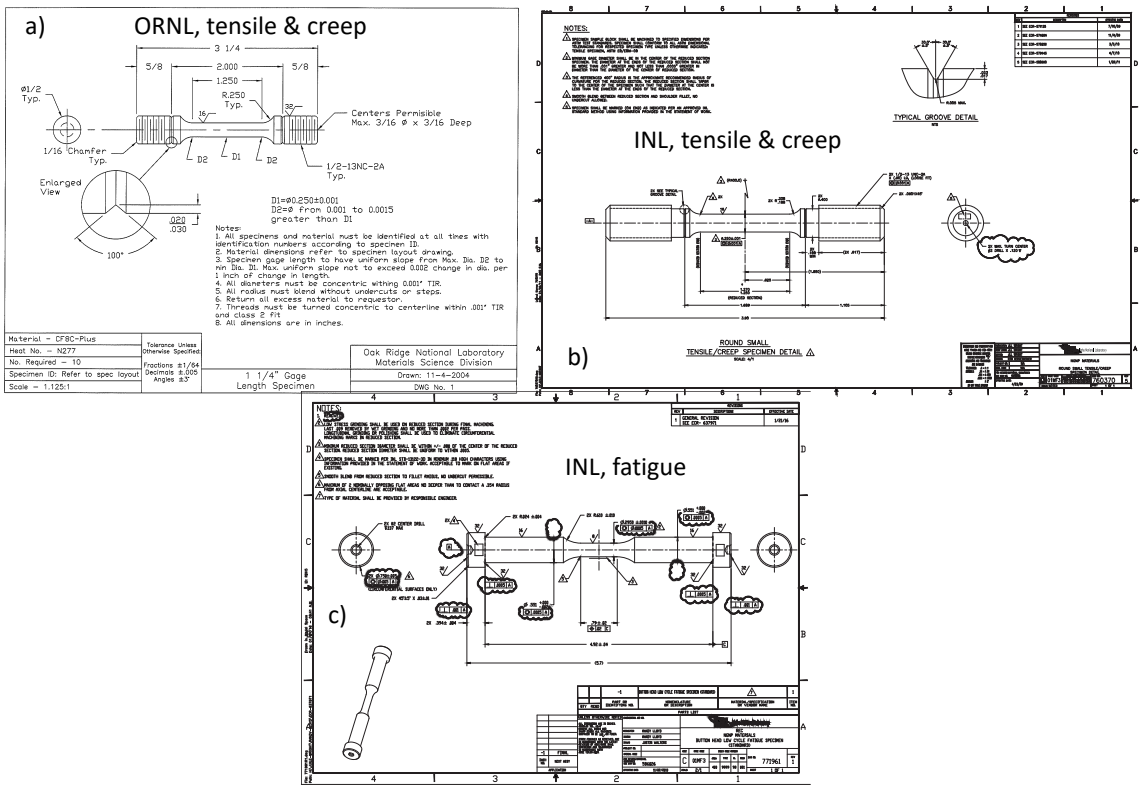

Figure 16: Geometry of the standard specimens, a) Tensile and creep, ORNL, b) Tensile and creep, INL, c) Fatigue and creep-fatigue, INL.

3.2.2.3 282 ranking

282 powder is a commercial product routinely produced by key manufacturers and alloy 282 will, therefore, obtain great scores in the powder manufacturing category. Due to the relatively low γ' content, ~20%, the alloy is relatively easy to print and hot cracking is not considered as a major challenge. An alloy density of > 99.5% [58-60] has been achieved by several teams, and a detailed description and quantification of all the defects in the LPBF 282 printed at ORNL will be achieved in FY23. Our current work has shown that a relatively large processing window exists (Figure 14) and complex LPBF 282 components such as heat exchangers have been fabricated [63-64]. The alloy will, therefore, also score well in the component manufacturing category. The PNNL materials scorecards report did not evaluate alloy 282 since the alloy is not currently considered for nuclear applications. The alloy is, however, well-known by the aerospace, gas turbines, SCO_2 and concentrated solar power communities with growing interest in LPBF 282. In addition to LPBF, several studies have investigated the microstructure, tensile properties, creep properties and crack propagation of alloy 282 fabricated by EBM [67-69]. Mechanical properties data is already available, mainly for tensile properties at room and high temperature, and the limited creep studies indicate that LPBF 282 should perform better at high temperature than alloy 617 (and likely LPBF 617). With the appropriate heat treatment, recrystallized microstructure with a high density of nano strengthening γ' precipitates can be achieved, similar to the wrought 282 microstructure. Our work in FY23 will generate crucial tensile, creep and fatigue data to improve the LPBF 282 scorecard and help determining if the alloy should be integrated into the AMMT program. Except for a few studies on the oxidation behavior at high temperature of LPBF 282 in air [70] or SCO_2 [64], no data exist on the environmental effects on LPBF 282. There is also no published work on digital manufacturing involving alloy 282 printing, but our current work aims at integrating LPBF 282 into the AMMT digital manufacturing framework using the Peregrine software.

3.2.3 Other high temperature alloys

3.2.3.1 Alloy 230

Alloy 230 (Ni-22Cr-14W-2Mo-0.02La) is a solution strengthened alloy developed by Haynes International with a high W content, known for its good oxidation resistance in various environments. Creep data from the Haynes database were added to the LMP plot in Figure 12 showing creep strength similar to the creep strength of alloy 617. The alloy is mainly used in the aerospace and power industries due to its microstructure stability and corrosion resistance at high temperature. 230 powder is a commercial product proposed by several powder manufacturers such as PAC, Hoganas and Oerlikon. Only a few recent studies have been published on AM 230 [71-73]. 230 powder was ordered from PAC and should be produced and delivered in August 2023. It will give us the opportunity to directly compare the microstructure, tensile and creep properties of LPBF 230 and LPBF 617, in addition to the current work on LPBF 282.

3.2.3.2 Alloy 740

Alloy 740 (Ni-24.5Cr-20Co-1.35Al-1.35Ti-1.5Nb) is a Ni-based γ' strengthened superalloy produced by Special Metals. The alloy is often compared to alloy 282 with similar creep strength and is considered for similar applications [50]. 740 powder is not currently a commercial product and it was decided to focus our attention and resources on alloy 282 in FY23. It is worth noting that a researcher from Special Metals attended the AMMT industrial workshop, highlighting a growing interest in AM technology from the company.

3.3 Low Cr Molten Salt Compatible Ni-based Alloys

3.3.1 Hastelloy N

Hastelloy N (Ni-7Cr-16Mo) was developed by ORNL for use in ORNL's Molten Salt Reactor and the alloy, with its low Cr content, continues to be a reference in terms of molten salt compatibility [74-75]. The alloy was extensively discussed in the PNNL materials scorecards report [8]. While the alloy scored well in the "Programmatic Factors" category due to its importance for molten salt reactors, the overall rating of the alloy was low since Hastelloy N powder is not a commercial product and very limited work has been conducted on Hastelloy N fabricated by AM. It is worth noting, however, that very recently Pillai et al. demonstrated the fabrication by DED of a graded structure, from the chemistry of Hastelloy N for molten salt compatibility to the chemistry of alloy 282 for high creep strength [76]. Discussion with Praxair was initiated to obtain a custom-made batch of Hastelloy N, but the delivery time will not allow the generation of relevant data in FY23.

3.3.2 Alloy 244

Alloy 244 (Ni-8Cr-22.5Mo-6W) was developed by Haynes as a high temperature low thermal expansion coefficient alloy. The low Cr content makes the alloy attractive to molten salt applications, and the creep data shown in Figure 12 highlights the alloy excellent creep strength, with lifetimes two order of magnitude longer compared to Hastelloy N when tested under similar conditions. One drawback is the high concentration of refractory elements leading to a higher cost. As for Hastelloy N, the alloy is not commercially available and no work has been conducted on AM 244. The fabrication for the first time by LPBF of the alloy is of interest for MSRs and INL will purchase 244 powder from Hoganas to be printed at ORNL. The goal is to assess the printability of the alloy, optimize the microstructure and generate tensile data. LPBF 244 should, offer much higher temperature capability in comparison to LPBF Hastelloy N.

4. Conclusion

Collaboration between the four " Prioritization of current reactor materials for advanced manufacturing" work packages has led to the definition of a decision criteria matrix allowing the systematic evaluation of nuclear candidate materials based on their technological readiness levels and their relevance to the nuclear industry and the AMMT program. This report was focused on, low Co, high temperature, and molten salt compatible Ni-based alloys. In-depth analysis of alloy 718 highlighted the high potential of LPBF 718, with the routine fabrication of complex components using commercial 718 powder, and mechanical properties comparable to the properties of wrought 718. We performed creep testing at 600-650°C on as printed and annealed LPBF 718 specimens and obtained lifetimes similar to the lifetimes of wrought 718, with properties slightly greater in the annealed recrystallized conditions. The presence of stable nano-size γ' and γ'' precipitates after the aging treatments explains the excellent strength of the alloy, and reducing the volume fraction of deleterious Laves and δ phases, in the grain and at grain boundaries, could lead in creep ductility improvement. The γ' strengthened alloy 282 was also evaluated due to its superior creep strength at high temperature compared to alloy 617 and 282 powder availability as a commercial product. While the alloy is not currently considered for nuclear applications, fabrication of complex LPBF 282 components has been achieved due to the great printability of the alloy when compared to other γ' superalloys. The alloy was produced at ORNL's MDF using a Renishaw 250 machine, and a central composite design approach was employed to determine the optimum printing parameters. Sufficient material has been produced to conduct tensile, creep and fatigue testing at both ORNL and INL and demonstrate the superior performance of LPBF 282 compared to (LPBF) 617 alloy. In-situ data generated

during printing will be analyzed with the Peregrine software and compared with CT scan measurements to demonstrate the integration of a new alloy into the AMMT digital manufacturing framework. Three additional Ni-based alloys, 625, 230, 617 will be printed in the near future to assess alloy printability and generate mechanical properties data not currently available. The results provided in this report will be combined with information from companion reports from INL, ANL and PNNL to generate a comprehensive document with detailed recommendations on the selection of alloys that could have a significant impact on the AMMT program.

5. Acknowledgements

The authors would like to thank K. Carver, J. Moser, D. Newberry, T. Lowe for their help with the experimental work and acknowledge H. Hyer and P. Fernandez-Zelaia for carefully reviewing the manuscript. This research was funded by the US Department of Energy, Office of Nuclear Energy, Advanced Materials and Manufacturing Technologies Program.

6. References

1. I. Gibson, D. Rosen, B. Stucker, M. Khorasani, “Additive Manufacturing Technologies”, Vol. 17 Springer (2021).
2. A. Ben-Ner and E. Siemsen, “Decentralization and Localization of Production: The Organizational and Economic Consequences of Additive Manufacturing (3D Printing)”, Managing Technology, 59, 5-23 (2017).
3. B. R. Betzler, B. J. Ade, P. K. Jain, A. J. Wysocki, P. C. Chesser, W. M. Kirkland, M. S. Cetiner, A. Bergeron, F. Heidet & K. A. Terrani, “Conceptual Design of the Transformational Challenge Reactor, Nuclear Science and Engineering”, 196, 1399-1424 (2022).
4. J. Haley, C. Leach, B. Jordan, R. Dehoff and V. Pacquit, “In-situ digital image correlation and thermal monitoring in directed energy deposition additive manufacturing”, Optics express, 29, 7, 9927-9941 (2021).
5. A. Huning. A. Smith, L. Scime, M. Russell, A. Coates, V. Paquit, R. Dehoff, “Advancement of Certification Methods and Applications for Industrial Deployments of Components Derived from Advanced Manufacturing Technologies”, ORNL report, ORNL/TM-2022/2654 (2022).
6. Z. Chen, C. Han, M. Gao, S. Y. Kandukuri and K. Zhou, “A review on qualification and certification for metal additive manufacturing”, Virtual and Physical Prototyping, 17:2, 382-405 (2022).
7. M. Li, D. Andersson, R. Dehoff, A. Jokisaari, I. Van Rooyen, and D. Cairns-Gallimore, “Advanced Materials and Manufacturing Technologies (AMMT), 2022 Roadmap”, ANL report, ANL-23/12 (2022).
8. T. Hartmann, S. Maloy and M. Komarasamy, “Materials Scorecards, Phase 2, Advanced Materials and Manufacturing Technology”, PNNL report, PNNL-32744 (2022).
9. M. Griffiths, Chapter 9, “Ni-based alloys for reactor internals and steam generator applications”, Structural Alloys for Nuclear Energy Applications, Edited by G.R. Odette and S.J. Zinkle (2019).
10. A. F. Rowcliffe, L. K. Mansur, D. T. Hoelzer, and R. K. Nanstad, "Perspectives on radiation effects in nickel-base alloys for applications in advanced reactors”, Journal of Nuclear Materials, vol. 392, 341-352 (2009).
11. M. Griffiths and R. Boothby, "Radiation Effects in Nickel-Based Alloys," in Comprehensive Nuclear Materials, 2nd ed, 334-371 (2020).
12. T. Yonezawa, "Nickel-Based Alloys," in Comprehensive Nuclear Materials, 7, 319-354 (2020).

13. A. Kracke, “Superalloys, the most successful alloy system of modern times – Past, Present and future”, Proceedings of the 7th International Symposium on Superalloy 718 and its derivatives, Edited by E.O Ott et al., TMS (The Minerals, Metals & Material Society), 13-50 (2010).
14. H. L. Eiselstein and D. J. Tillack, “The invention of and definition of alloy 625”, Superalloys 1992, Edited by E.A. Loria et al., 1-14 (1991).
15. https://www.additivemanufacturing.media/news/senvol-commercializes-siemens-energys-material-databases
16. https://www.makepartsfast.com/shell-and-ge-additive-show-joint-design-and-engineering-project-at-formnext/
17. https://www.ge.com/additive/press-releases/turn-larger-lighter-additive-parts
18. S. Taller, A. Le Coq, C. Massey, J. Werden, M. Lynch and K. Linton, “ Report on Evolution of Inconel 718 Following HFIR Irradiation”, ORNL report, ORNL/TM-2022/2600 (2022).
19. https://www.praxairsurfacetechnologies.com/en/materials-and-equipment/materials/additive-manufacturing-powders?tab=truform-product-portfolio
20. https://www.carpenteradditive.com/metal-powders/high-temperature-nickel-base
21. S. Sanchez, P. Smith, Z. Xu, G. Gaspard, C. J. Hyde, W. W. Wits, I.A. Ashcroft, H. Chen, A. T. Clare, “Powder Bed Fusion of nickel-based superalloys: A review”, International Journal of Machine Tools & Manufacture, 165, 103729 (2021).
22. S. Catchpole-Smith, N. Aboulkhair, L. Parry, C. Tuck, I.A. Ashcroft, A. Clare, “Fractal scan strategies for selective laser melting of ‘unweldable’ nickel superalloys”, Additive Manufacturing 15, 113–122 (2017).
23. K. Moussaoui, W. Rubio, M. Mousseigne, T. Sultan, F. Rezai, “Effects of Selective Laser Melting additive manufacturing parameters of Inconel 718 on porosity, microstructure and mechanical properties”, Mater. Sci. Eng. A 735, 182–190 (2018).
24. A. Hilaire, E. Andrieu, X. Wub, “High-temperature mechanical properties of alloy 718 produced by laser powder bed fusion with different processing parameters”, Additive Manufacturing, 26, 147–160 (2019).
25. K. Gruber a, W. Stopyra, K. Kobiela, B. Madejski, M. Malicki, T. Kurzynowski, “Mechanical properties of Inconel 718 additively manufactured by laser powder bed fusion after industrial high-temperature heat treatment”, Journal of Manufacturing Processes, 73, 642–659 (2022).
26. E. M. Fayed, M. Saadati, D. Shahriari, V. Brailovski, M. Jahazi, & M. Medraj, “Effect of homogenization and solution treatments time on the elevated-temperature mechanical behavior of Inconel 718 fabricated by laser powder bed fusion”, Scientific Reports, 11:2020 (2021).
27. S. Taller and T. Austin, “Using post-processing heat treatments to elucidate precipitate strengthening of additively manufactured superalloy 718”, Additive Manufacturing”, 60, 103280 (2022).
28. M. Komarasamy, S. Shukla, S. Williams, K. Kandasamy, S. Kelly, R.S. Mishra, “Microstructure, fatigue, and impact toughness properties of additively manufactured nickel alloy 718”, Additive Manufacturing 28, 661-675, (2019).
29. Y. Gao, D. Zhang, M. Cao, R. Chen, Z. Feng, R. Poprawe, J.H. Schleifenbaum, S. Ziegler, “Effect of δ phase on high temperature mechanical performances of Inconel 718 fabricated with SLM process”, Mater. Sci. Eng. A. 767, 138327 (2019).
30. E. Hosseini and V.A. Popovich, “A review of mechanical properties of additively manufactured Inconel 718”, Additive Manufacturing, 30, 100877 (2019).
31. L. Huang, Y. Cao, J. Zhang, X. Gao, G. Li, Y. Wang, “Effect of heat treatment on the microstructure evolution and mechanical behaviour of a selective laser melted Inconel 718 alloy”, Journal of Alloys and Compounds 865, 158613 (2021).
32. S. Okazaki, O. Takakuwa, Y. Ogawa, Y. Funakoshi, H. Kawashima, S. Matsuoka, H. Matsunaga, “Defect tolerance and hydrogen susceptibility of the fatigue limit of an additively manufactured Ni-based superalloy 718”, International Journal of Fatigue 139, 105740 (2020).

33. S. Sanchez, C. Hyde, I. Ashcroft, G. Ravi, A. Clare, “Multi-laser scan strategies for enhancing creep performance in LPBF”, Additive Manufacturing 41, 101948 (2021).
34. M. Chang, A.K. Koul, P. Au, and T Terada, “Damage Tolerance of Wrought Alloy 718 Ni.Fe-Base Superalloy”, Journal of Materials engineering and Performance, 3, 356-366 (1994).
35. C. R. Brinkman’, M. K. Booke, and J. L. Ding, “Creep and Creep-rupture behavior of alloy 718”, Proceedings of Superalloys 718,625 and Various Derivatives, Edited by Edward A. Iaria, The Minerals, Metals & Materials Society, 519-536 (1991).
36. Y.-L. Kuo, S. Horikawa, K. Kakehi, “Effects of build direction and heat treatment on creep properties of Ni-base superalloy built up by additive manufacturing”, Scripta Materialia 129, 74–78 (2017).
37. Y.-L. Kuo, T. Nagahari, K. Kakehi, “The effect of post-processes on the microstructure and creep properties of Alloy718 built up by selective laser melting”, Materials 11 (6) (2018) 996.
38. S. Wu, H.Z. Peng, X. Gao, P.D. Hodgson, H.Y. Song, Y.M. Zhu, Y. Tian, A.J. Huang, “Effect of heat treatment on microstructure evolution of Inconel 718 alloy fabricated by selective laser melting”, Journal of Alloys and Compounds 764, 639-649 (2018).
39. X. Li, J.J. Shi, C.H. Wang, G.H. Cao, A.M. Russell, Z.J. Zhou, C.P. Li, G.F. Chen, “Effect of heat treatment on microstructure evolution of Inconel 718 alloy fabricated by selective laser melting”, Journal of Alloys and Compounds, 764, 639–649 (2018).
40. F. Bachmann, R. Hielscher, H. Schaeben, “Texture analysis with MTEX- Free and open-source software toolbox”, Solid State Phenom, 160, 63–68 (2010).
41. M.M.Kirka, F. Medinac,R. Dehoff, A. Okello, “Mechanical behavior of post processed Inconel 718 manufactured through the electron beam melting process”, Materials Science & Engineering A 680, 338–346 (2017).
42. S. Pratheesh Kumar, S.Elangovan, R.Mohanraj, J.R.Ramakrishna, “A review on properties of Inconel 625 and Inconel 718 fabricated using direct energy deposition”, Materials Today: Proceedings 46, 7892–7906 (2021).
43. X. Xu, J. Ding, S. Ganguly, S. Williams, “Investigation of process factors affecting mechanical properties of INCONEL 718 superalloy in wire + arc additive manufacture process”, Journal of Materials Processing Tech., 265 201–209 (2019).
44. P. Nandwana,A. M.Elliott, D. Siddel, A. Merriman,W. H.Peter, S., S. Babu, “Powder bed binder jet 3D printing of Inconel 718:Densification, microstructural evolution and challenges”, Current Opinion in Solid State and Materials Science 21, 207–218 (2017).
45. J. Yang, X. Liu, M. Song, L. He, S. Bankson, M. Hamilton, B. Prorok, X. Lou, “Sensitization, desensitization, and carbide evolution of Alloy 800H made by laser powder bed fusion”, Additive Manufacturing 50, 102547 (2022).
46. J. Yang, M. Song, L.R. Hawkins, X. Liu, L. He, X. Lou, “Effects of heat treatment on corrosion fatigue and stress corrosion crack growth of additive-manufactured Alloy 800H in high-temperature water”, Corrosion Science, 191, 109739 (2021).
47. T. Hassel1 & T. Carstensen, “Properties and anisotropy behaviour of a nickel base alloy material produced by robot-based wire and arc additive manufacturing”, Welding in the World, 64, 1921–1931 (2020).
48. B. Avinash , K. Manikanda Subramanian, and V. Rajkumar, “Microstructure, Mechanical Properties and Corrosion Behavior of Inconel 617 Superalloy Fabricated by Wire Arc Additive Manufacturing”, Journal of Materials Engineering and Performance, 32, 6270–6280 (2023).
49. L.M. Pike, “Development of a fabricable gamma-prime ($\gamma 0$) strengthened superalloy”, in: R.C. Reed, K.A. Green, P. Caron, T.P. Gabb, M.G. Fahrmann, E.S. Huron, Shiela A. Woodard (Eds.), In Superalloys 2008, 191–200 (2008).
50. R. Viswanathan, J. Shingledecker, and R. Purgert, “Evaluating Materials Technology for Advanced Ultrasupercritical Coal-Fired Plants,” Power 154, 41-45 (2010).
51. Jablonski, P.D., Hawk, J.A., Cowen, C.J., Maziasz, P.J., “Processing of Advanced Cast alloys for A-USC Steam Turbine Applications”, JOM, 64, 271-279 (2012).

52. Shen C., “Modeling Creep-Fatigue-Environment Interactions in Steam Turbine Rotor Materials for Advanced Ultra-supercritical Coal Power Plants”, GE Global Research Final Report, DOE/NETL Cooperative Agreement DE-FE0005859 (2014).
53. B. A. Pint, Hong Wang, C. Shane Hawkins, Kinga A. Unocic, “Technical Qualification of New Materials for High Efficiency Coal-Fired Boilers and Other Advanced FE Concepts: Haynes® 282® ASME Boiler and Pressure Vessel Code Case”, ORNL report, ORNL/TM-2020/1548 (2020).
54. R. Wright, “Draft ASME Boiler and Pressure Vessel Code Cases and Technical Bases for Use of Alloy 617 for Constructions of Nuclear Component Under Section III, Division 5”, INL report, INL/EXT-15-36305 Revision 2 (2021).
55. B. A. Pint and J. R. Keiser, “Effect of Pressure and Thermal Cycling on Long-Term Oxidation in Supercritical CO_2,” NACE Paper C2019-12750, Houston, TX, presented at NACE Corrosion 2019, Nashville, TN (2019).
56. V. P. Deodeshmukh and B. A. Pint, “Long-Term Performance of High Temperature Alloys in Oxidizing Environments and Supercritical CO_2,” in Proceedings of the Joint EPRI – 123HiMAT International Conference on Advances in High Temperature Materials, J. Shingledecker and M. Takeyama eds., ASM International, Materials Park, OH, 2020, pp. 953-966.
57. R. Pillai, M. Romedenne and S. Lee, “Development of an Open-source Alloy selection and Lifetime assessment tool for structural components in CSP”, ORNL report, ORNL/TM-2021/2365 (2021).
58. Z. Islam, A. Kumar, A.B. Rankouhi, C. Magnin, M.H. Anderson, F.E. Pfefferkorn and D.J. Thoma, “A High-Throughput Method to Define Additive Manufacturing Process Parameters: Application to Haynes 282”, Metallurgical and Materials Transactions A, 53, 250-263 (2022).
59. A. S. Shaikh, F. Schulz, K. Minet-Lallemand, E. Hryh, “Microstructure and mechanical properties of Haynes 282 superalloy produced by laser powder bed fusion”, Materials Today Communications, 26, 102038 (2021).
60. J. Boswell, J. Jones, N. Barnard, D. Clark, M. Whittaker, R. Lancaster, “The effects of energy density and heat treatment on the microstructure and mechanical properties of laser additive manufactured Haynes 282”, Materials & Design 205, 109725(2021).
61. K.A. Christofidou, H.T. Pang, W. Li, Y. Pardhi, C.N. Jones, N.G. Jones, H.J. Stone, “Microstructural control and optimization of Haynes 282 manufactured through laser powder bed fusion”, in: S. Tin, M. Hardy, J. Clews, J. Cormier, Q. Feng, J. Marcin, C. O’Brien, A. Suzuki (Eds.), Superalloys 2020, Springer International Publishing, Cham, 1014–1023 (2020).
62. K.A. Unocic, D. Shin, X. Sang, E. Cakmak, P.F. Tortorelli, “Single-step aging treatment for a precipitation-strengthened Ni-based alloy and its influence on high-temperature mechanical behavior”, Scripta Materialia 162, 416–420 (2019).
63. R. Rajan, Raytheon Technologies Research Center “Developing an Ultra-Compact, Topology-Optimized Heat Exchanger using Additive Manufacturing”, ARPA-E project.
64. C. Magnin, Z. Islam, M. Elbakhshwan, A. Brittan, D. J. Thoma. M. H.Anderson, “The performance of additively manufactured Haynes 282 in supercritical CO_2”, Materials Science & Engineering A 841, 143007 (2022).
65. L. Scime J. Haley V. Paquit, “Summary of Methodology for Mitigating Risks Associated with Licensing and Qualifying AM Nuclear Materials”, ORNL report, ORNL/SPR-2019/1355 (2019).
66. H. C. Hyer, D. C. Sweeney Christian M. Petrie, “Summary of Methodology for Mitigating Risks Associated with Licensing and Qualifying AM Nuclear Materials”, ORNL report, ORNL/TM-2023/2851 (2023).
67. K.A. Unocic, M.M. Kirka, E. Cakmak, D. Greeley, A.O. Okello, S. Dryepondt, “Evaluation of additive electron beam melting of Haynes 282 alloy”, Materials Science & Engineering A 772, 138607 (2020).
68. S. Dryepondt, M. M. Kirka, P. Fernandez-Zelaia and K. A. Unocic, “Microstructure and mechanical properties of Haynes 282 Fabricated by Electron Beam Melting”, Joint EPRI-

123HiMAT International Conference on Advances in High-Temperature Materials, edited by John Shingledecker and Masao Takeyama (2019).
69. P. Fernandez-Zelaia, J. O. Rojas, J. Ferguson, S. Dryepondt, and M. M. Kirka, “Fatigue crack growth resistance of a mesoscale composite microstructure Haynes 282 fabricated via electron beam melting additive manufacturing”, Journal of Materials Science, 57, 9866–9884 (2022).
70. M. Romedenne, P. Stack, R. Pillai and S. Dryepondt, “Isothermal and Cyclic Oxidation of Haynes 282 Processed by Electron Beam Melting (EBM) and Laser Powder Bed Fusion (LPBF) in Dry Air at 800 and 950°C”, JOM, 74, 1707-1718 (2022).
71. K. Momeni, “Sensitivity of laser powder bed fusion additive manufactured HAYNES230 to composition and print parameters”, Journal of materials research and technology, 15, 6453-6463 (2021).
72. Y. Zhao, Z. Ma, L. Yu, Y. Liu, “New alloy design approach to inhibiting hot cracking in laser additive manufactured nickel-based superalloys”, Acta Materialia 247, 118736 (2023).
73. X. Liu, R. Hu, X. Luo, C. Yang, X. Gao, “ A high-strength Ni–Cr–W based superalloy prepared by laser powder bed fusion: printability, microstructure and tensile properties”, Materials Science & Engineering A, 853, 143744 (2022).
74. T. K. Roche, The Influence of Composition Upon the 1500°F Creep-Rupture Strength and Microstructure of Molybdenum-Chromium-Iron-Nickel-Base Allovs, ORNL report 2524 (1958).
75. R.W. Swindeman, The mechanical properties of INOR-8, ORNL report, ORNL-2780 (1961).
76. R. Pillai, Q.Q. Ren, Y-F. Su, R. Kurfess, T. Feldhausen, S. Nag, “Leveraging additive manufacturing to fabricate high temperature alloys with co-designed mechanical properties and environmental resistance”, Proceedings of ASME Turbo Expo 2023, Boston MA, GT2023-103009 (2023).